Modeling and Propagation Characterization of THz Wireless Links in Computer Desktop Environment

Jinbang Fu, Prateek Juyal, and Alenka Zajić
*

Georgia Institute of Technology, Atlanta, GA 30332 USA

Key Points:

- The THz measurements have been conducted in the novel motherboard desktop environment.
- We proposed a comprehensive THz wireless channel model which includes the mean path loss model, the Gamma-mixture model, and the modified S-V model.
- The results measured in free-space and the motherboard desktop environment have been compared and analyzed.

*This work has been supported, in part, by NSF grant 1651273. The views and findings in this paper are those of the authors and do not necessarily reflect the views of NSF.

Corresponding author: Jinbang Fu, jfu72@gatech.edu

Abstract

In this paper, THz channel propagation characterization and modeling for a desktop environment is presented. Path loss and PDPs measured on the motherboard in both free-space and desktop resemble metal cavity are compared. To characterize the large scale fading of the channel, mean path loss model as a function of antenna height is proposed by treating the motherboard desktop environment as a partially dielectric filled resonant cavity. Good match between the measured and modeled path loss proves the model validity. For the shadowing across the frequency, Gamma-mixture model is applied to characterize the oscillations of in-cavity measured path loss. Results show that with proper choice of the number of mixed Gamma distributions k, the goodness of fit between the model and the probability density function (PDF) of path loss oscillations can reach more than 97%. Multipath components are characterized by cluster-based channel modeling. Modifications were made on the conventional S-V model to accurately characterize the channel by rewriting the cluster power decay with step-wise functions and each sub-function is expressed exponentially in dB, and the ray power decay with power law approach. A good agreement can be observed between the model and the measurements.

1 Introduction

The deployment of 5G cellular network and the application of WIFI 6 make the wireless networks' data rate reach several tens of gigabits per second. The high-speed and low latency communications foster the growth of IoT applications such as home automation, wearable technology, smart healthcare, vehicular communication systems, and inter-chip communications. In the past three years, the number of active IoT devices increased from 7.7 to 10 billion, and this number will surpass 25 billion by 2030 from the estimation (Statista, 2021). The explosive growth of IoT requires significant increase in data transfer and storage. The data volume of IoT is about 13.6 zettabytes in 2019 and expected to reach 79.4 zettabytes by 2025 (Statista, 2019). This large amount of data requires better rack-to-rack, device-to-device, and chip-to-chip communications which increasing the demand for more bandwidth. As there is no available bandwidth wider than 10 GHz below 100 GHz (Tekbıyık et al., 2019), the frequency limits was pushed to terahertz band, which is between 0.1 THz to 10 THz (Tekbıyık et al., 2021).

For chip-to-chip communication, THz wireless communication has been considered as a future solution. With wireless communication, the pain of cable management and the complex system design can be alleviated. At THz frequency, larger available bandwidth can help shrink the gap of the data rate between wired and wireless communications(Kürner, 2018), also, smaller antenna and antenna spacing are required, which means that more antennas can be integrated on a single chip to provide additional links.

To design a THz wireless chip-to-chip communication system, the wireless channel should be proper characterized and modeled first, then, other parts can be designed accordingly. A large number of THz indoor measurements have been performed to characterize line-of-sight (LoS) and non-LoS (NLoS) propagation, the effects of shadowing and angles of departure and arrival, and the reflection and diffraction from different materials (Khalid & Akan, 2016; Kim & Zajić, 2015, 2016; Priebe et al., 2011, 2010; Jacob et al., 2012; Kleine-Ostmann et al., 2012; Fricke et al., 2013, 2015; Cheng et al., 2018; Cheng & Zajić, 2018; Cheng et al., 2020). Also, the characterization of wave-guide structure with different dimensions has been done at 60 and 300 GHz (Kürner et al., 2015). Moreover, THz measurements have been conducted on the motherboard in free-space with the consideration of LoS, NLoS, reflected-NLoS (RNLoS), and obstructed-LoS (OLoS) propagation (Kim & Zajić, 2016). Furthermore, the wireless channel characterizations at 300 GHz have been performed inside a desktop metal cavity and a nettop size metal case (Fu et al., 2019a, 2019b; Fu et al., 2021).

According to the characterized propagation mechanisms, some THz path loss models have been proposed as the combination of propagation loss and the attenuation of molecular absorption (Jornet & Akyildiz, 2011; Schneider et al., 2012). Considering the attenuation and scattering effect of air and leaves, the path loss through the vegetation has been modeled in (Afsharinejad et al., 2015). Also, the performance of several large scale path loss models has been tested at 30, 140, and 300 GHz (Cheng et al., 2017). For in-cavity scenarios, path loss model has been proposed as the summation of spreading loss, resonant-based power variation, and the loss due to the radiation pattern of antenna in (Fu et al., 2020, 2021). Similarly, several stochastic THz wireless channel models have been raised for indoor scenarios to capture the multipath fading (He et al., 2017; Priebe & Kürner, 2013; Priebe et al., 2014; Kim & Zajić, 2015, 2016; Piesiewicz et al., 2007; Fricke et al., 2017; Priebe et al., 2011). Considering the ultra-wide bandwidth and rapid change of THz wireless channel, the Gamma-mixture model has been proposed in (Tekbıyık et al., 2021; Al-Hmood, 2017). In addition, S-V model has been applied to model the THz wireless channel in a data center (Cheng et al., 2020). Furthermore, the geometry based statistical THz channel models inside a desktop size and a nettop size metal cavity have been proposed in (Fu et al., 2021, 2020).

Channel characterization and modeling is the first step to build the inter-chip communication network inside a computing system. Even though channel measurements and modelings have been performed in free-space on the motherboard (Kim & Zajić, 2016; Kim & Zajić, 2016) and inside a desktop size metal cavity and a nettop size metal enclosure with components measured separately (Fu et al., 2019b; Fu et al., 2020, 2021), the on-board THz channel characterization and modeling in a desktop environment have not been done yet. This paper is trying to fill the gap. We fixed a motherboard inside a desktop size metal enclosure to simulate a practical desktop environment and performed measurements on the motherboard in both free-space and the metal cavity with the consideration of several potential propagation scenarios: LoS over the motherboard, RN-LoS propagation with vertical plugged dual in-line memory module (DIMM) as the reflector, OLoS with the obstruction of parallel plugged DIMMs, NLoS propagation with the signal being blocked by a heat sink, and a practical CPU-PCI link. The contributions of this paper are:

1. The THz channel measurements have been conducted in the novel motherboard desktop environment. The finding of channel characteristics can be applied for the design of on-board chip-to-chip communication system.
2. A comprehensive THz wireless channel model for the motherboard desktop environment is first proposed. We modeled the path loss and PDP of the channel, respectively. For the path loss, A new mean path loss model for the novel desktop environment is proposed. By treating the complex motherboard as dielectric slab, we modeled the environment as a partially dielectric filled cavity and thereby extracted the path loss parameters using the resonant mode analysis. Also, Gamma-mixture model is proposed to describe the shadowing across the frequency by modeling the probability density function (PDF) of path loss oscillations over the measured band. Sensitive and Vulnerable THz signal performs differently on different sections of the ultra-wide band. Hence, mixture model is necessary. These proposed models explain the propagation loss of THz channel in the motherboard desktop environment. For the PDP, a modified cluster based S-V model is introduced to describe the multipath components of the channel. Unlike the conventional Saleh-Valenzuela (S-V) model, neither the cluster power nor the ray power follows the assumed exponential decay in our measurements. To better characterize the channel and more accurately describe the results, we modified the cluster power decay with step-wise functions with each sub-function expressed exponentially in dB, and the ray power decay with the power law-approach.
3. The path loss and PDPs measured in free-space and inside the metal cavity are compared. Similar trend of mean path loss behavior can be observed in free-space

and inside the cavity. Strong oscillations of the path loss over the THz band can be seen in both scenarios due to the scatterings on the components. Because of the effects of resonant modes, signal oscillates more rapidly and randomly inside the motherboard desktop environment, and more multipath components can be observed from the in-cavity measured PDP plots.

The rest of this paper is organized as follows. Section 2 describes the equipment and the measurements setup. Section 3 introduces the details of the investigated potential scenarios. The channel modeling is presented in Section 4. The result analysis and model verification are shown in Section 5. Finally, Section 6 draws the concluding mark.

2 Measurement Setup

The Measurement setup includes a Keysight N5224A PNA vector network analyzer (VNA), a Virginia Diodes, Inc. (VDI) transmitter (Tx210) and a VDI receiver (Rx148)(Virginia Diodes, n.d.-a). The VNA generates the input signal in the range of 10 MHz to 12 GHz with the power level (P_{in}) of 0 dBm and feeds it in to the VDI Tx210. In the VDI Tx210 transmitter, a 25 GHz signal is generated by a Herley-CTI phase-locked dielectric resonator oscillator (DPRO with 100 MHz reference crystal oscillator)(Communications, n.d.). It is amplified and frequency doubled by Norden N08-1975(Millimeter, n.d.), and then tripled by VDI WR6.5X3(Virginia Diodes, n.d.-c). This signal is then fed into a sub-harmonic mixer (WR2.8SHM)(Virginia Diodes, n.d.-b) which doubles the carrier frequency and mixes it with the VNA generated baseband signal. This terahertz-range signal is then transmitted by a horn antenna in the range of 280-320 GHz. Same components are used to down-convert the signal, except that the DPRO is tuned to 24.2 GHz. The received signal is then down-converted to an intermediate frequency (IF) of 9.6 GHz. The VNA then samples the upper sideband of the down converted signal in the range of 9.61-29.6 GHz with 801 points. The block diagram of the measurement system is shown in Fig. 1 and all measurement parameters are summarized in Table. 1.

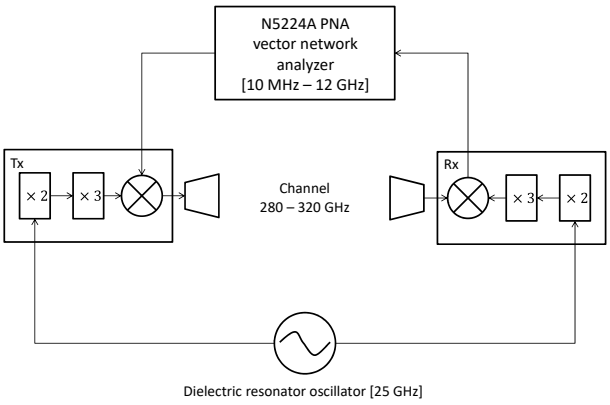

Figure 1. Block diagram of the measurement system.

Pyramid horns with the gain varies in the range of 22 to 23 dBi over the observed frequency band from 300 to 312 GHz were used in the measurements. The theoretical half power beam-width (HPBW) of the horn is about 12°in azimuth and elevation. The physical dimension of the horn aperture is 8.91 mm, which limits the far-field boundary to be 15.88 cm at 300 GHz according to the Fraunhofer distance.

Table 1. Measurement Parameters

Parameter	Symbol	Value
Measurement points	N	801
Intermediate frequency bandwidth	Δf_{IF}	20 kHz
Average noise floor	P_{N}	-90 dBm
Input signal power	P_{in}	0 dBm
Start frequency	f_{start}	10 MHz
Stop frequency	f_{stop}	12 GHz
Bandwidth	B	11.99 GHz
Time domain resolution	Δt	0.083 ns
Maximum excess delay	τ_{m}	33.4 ns

3 Measurement Scenarios inside Desktop in Comparison with Free-Space

To simulate the desktop environment, an aluminum metal cavity with the size of $27.5 \times 27.5 \times 10$ cm was fabricated. As shown in Fig. 2a, two square aluminum plates with the length of 27.5 cm were spaced by eight 5 cm long Nylon hex standoffs (Electronics, n.d.-b) with two piled up at each corner and fixed by eight 2 cm long Nylong standoffs (Electronics, n.d.-a), which formed as the top and bottom walls of the cavity. The other four sides of the metal cavity were wrapped by aluminum foils and labeled as A, B, C, and D, as shown in Fig. 2a. The fabricated cavity approximates a computer desktop casing. Inside the fabricated case, as shown in Fig. 2b, a motherboard was supported on the bottom wall of the cavity by four groups of brass 14 mm+6 mm male hex standoffs (Inc., n.d.) with each group formed by 3 standoffs piled up and was fixed by other four brass standoffs and four screws on the other side of the bottom wall and the motherboard, respectively. For all the scenarios addressed in this paper, measurements were performed on the motherboard inside the fabricated metal cavity and in free-space as comparison.

3.1 LoS Link

To develop a complete THz wireless communication scheme for computing system, it is necessary to understand the propagation mechanisms under the specific environment. LoS propagation is the first scenario being considered. Different with other LoS links in free-space where antennas are elevated high enough so that ground has little effect to the link, for the wireless communication in computing system, antennas are always mounted on chips which are very close to the motherboard. Apart from the ground effects due to the motherboard, the resonant modes effects inside casing (Fu et al., 2019b; Fu et al., 2020, 2021) cannot be avoided. During the measurements, as shown in Fig. 3, the fabricated cavity with motherboard fixed inside was put in between the transmitter (Tx) and receiver (Rx) with antennas aligned horizontally. Two square openings with the horn size were drilled align the middle lines on the transceiver sidewalls (side A and C) of the cavity according to the antennas' heights. To simulate the communication inside desk-

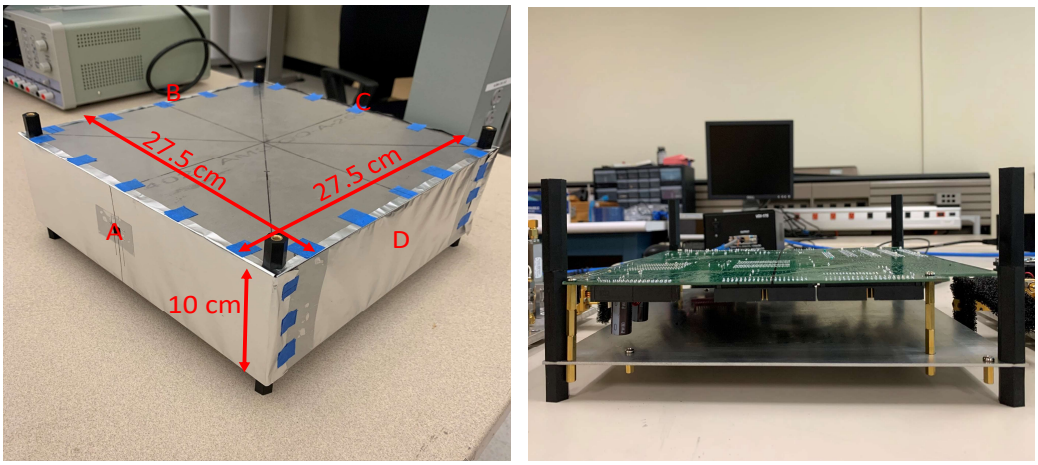

(a) (b)

Figure 2. Simulated desktop environment (a) fabricated metal casing (b) motherboard used in measurements.

top, antennas were inserted into the cavity through the drilled holes. The length of the equipped horns is about 42.08 mm, which implies that the distance between two horns, d, is about 19.1 cm. To characterize the ground effect of the motherboard and the resonant modes inside the cavity, measurements were performed by vertically moving the transceivers simultaneously with the antenna height, h, varying from 0 cm to 4.5 cm, while keeping the distance $d = 19.1$ cm. To separate the influence of the motherboard from the effect of other components on the mother board, the backside of the motherboard was used for investigation. Please note that the parameter h indicates the distance between the bottom edge of horn to the motherboard, and $h = 0$ cm indicates that the horn touches the surface of the motherboard. The distance between the phase center and bottom edge of the horn is about 4.46 mm.

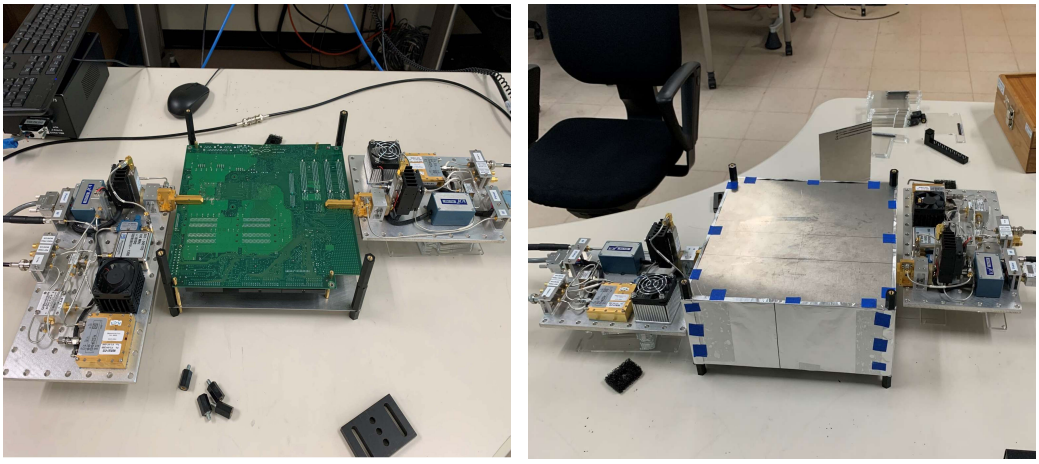

(a) (b)

Figure 3. LoS measurement scenario (a) in free-space (b) inside the metal cavity.

3.2 RNLoS Link

Owing to the high density of the components, clear LoS propagation path on the motherboard has a low probability. As one of the possible major obstruction, DIMM was investigated as a reflector to connect the Tx and Rx which are orthogonal to each other as it was vertically plugged on the mother board. As shown in Fig. 4a, the DIMM was vertically put on the center of the motherboard and diagonally aligned with transceivers. The distance from the DIMM to each of the transceiver is equal to $d/2 = 9.55$ cm. Measurements have been performed both in free-space and inside the metal cavity on the backside of the motherboard with the antenna height $h = 1.8$ cm. For the cavity measurement, antennas were inserted into the cavity through two horn-size square holes drilled on the sidewall A and D of the cavity as shown in Fig. 4b. Both flat side and component side of the DIMM were measured.

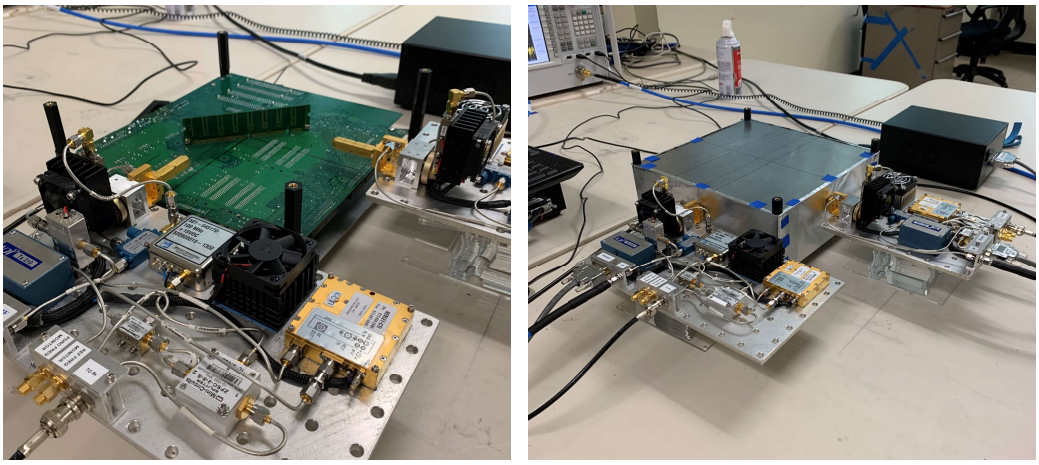

(a) (b)

Figure 4. RNLoS measurement scenario (a) in free-space (b) inside the metal cavity.

3.3 OLoS Link

A practical scenario for on-board wireless communication is the LoS link being perturbed by parallel-plate structure which could be possible served as a parallel wave-guide. To investigate the effects of parallel-plate structure on the motherboard , we performed measurements with two DIMMs being put in parallel on the center of the motherboard's backside as shown in Fig 5. During the measurements, the distance between parallel DIMMs, w, was varied from 2 cm to 7 cm while keeping the antenna height $h = 1.8$ cm to see how path loss changes with the variation of w.

3.4 OLoS Link

On the motherboard. some big components like the heatsink which transfers the heat generated by electronic devices can block most LoS signals. However, some small openings on the components like the gaps between fins of the heatsink can still make the communication possible. Therefore, We made measurements with a heatsink as the obstruction to see how it affects the wireless link. Figure 6 shows the setup of the measurements. As shown in Fig. 6, a heatsink with the size of $3.5 \times 3.1 \times 2.3$ cmwere put on the center of motherboard's backside. The distance from the heatsink to each of the transceiver is about 8.1 cm. To fully understand how wireless link is affected by the gaps between

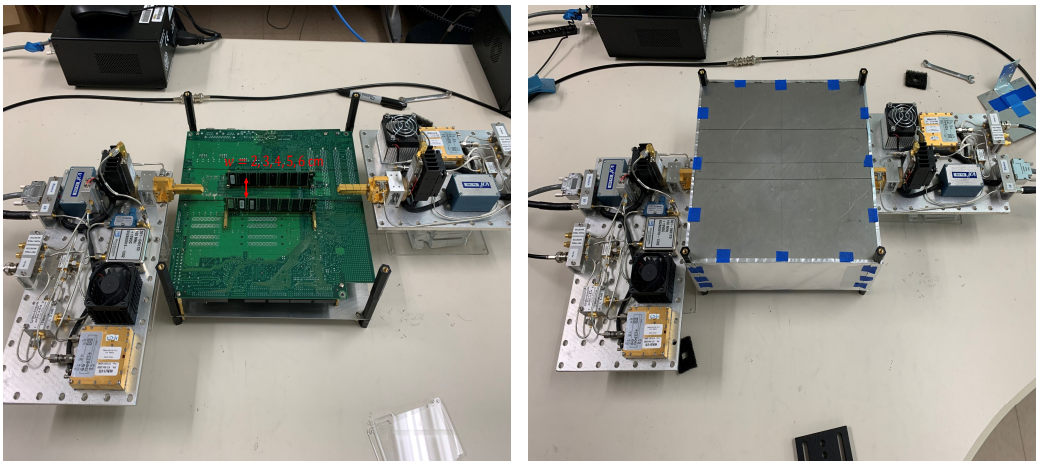

(a) (b)

Figure 5. OLoS measurement scenario (a) in free-space (b) inside the metal cavity.

fins of the heatsink, measurements were performed by horizontally moving the heatsink away from the transceiver towards the side D of the cavity with step increment of 0.25 cm. The antenna height was kept at 1.8 cm same as the setup in previous measurements.

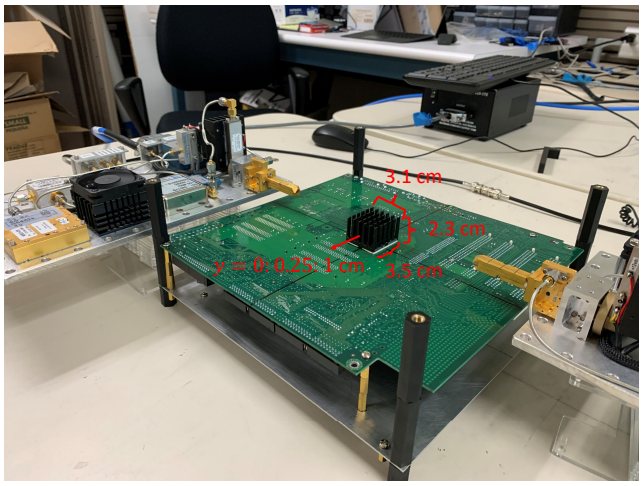

Figure 6. NLoS measurement scenario.

3.5 CPU-PCI Link

After the investigation of several possible scenarios on the motherboard separately, a practical link on the densely populated front side of the motherboard was measured. As shown in Fig. 7, the potential CPU-PCI (Peripheral Component Interconnects) link was measured in both free-space and metal cavity with the setup shown in the Fig. 7, where the Tx was mounted on the top of the CPU and Rx was hung over the PCI slots with 19.3 cm T-R separation. Since other hardware components like network cards, sound cards, disk controllers are always vertically plugged on the PCI slots, we set a 3 cm T-

R vertical misalignment to approximate the height difference between the CPU and the chip on the peripheral components. It can be observed from the figure that there are several PCI slots on the mother board with different distances to the CPU. Hence, measurements were performed by gradually increasing the T-R separation to 23.3 cm with the step increment of 1 cm while keeping the T-R vertical misalignment of 3 cm.

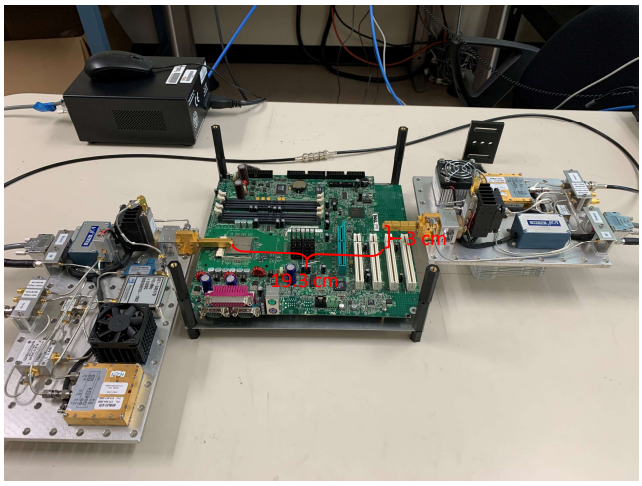

Figure 7. CPU-API link scenario.

4 Channel Modeling

To comprehensively describe the wireless channel in the motherboard desktop environment, we modeled the path loss and PDP which describe the signal attenuation and the multipath components of the channel, respectively, under the potential scenarios described in Section 3. For the stationary multipath propagation channel, the time-invariant delay spread function can be written as

$$h(\tau) = A \sum_{n=1}^{N} c_n e^{j\phi_n} \delta(\tau - \tau_n), \tag{1}$$

where the N is the number of propagation paths, c_n is the normalized amplitude associate with the n^th propagation path, ϕ_n is the phase delay of the n^th component and can be modeled as a random variable uniformly distributed in $[-\pi, \pi)$, and τ_n is the time delay of the multipath component. The envelope power of the channel response $A^2 = |h(\tau)|^2 = \mathrm{P_t G_t G_r / PL}$ follows the mixed Gamma distribution, where $\mathrm{Pt}, \mathrm{G_t}, \mathrm{G_r}$, and PL are the transmit power, Tx antenna gain, Rx antenna gain, and the path loss, respectively. The path loss includes the mean path loss over the measured band which is modeled by the proposed mean path loss model as a function of antenna height for the large scale fading of the channel, and the shadowing across the frequency which is described by the Gamma-mixture model by capturing the PDF of path loss variations. The PDP is referred as the squared amplitude of the channel response and can be modeled by the modified S-V model for THz wireless channel in motherboard desktop environment.

4.1 Mean Path Loss Model for Averaged Path Loss Variations w.r.t the Antenna Height

Mean value of the measured path loss by averaging over the frequency band varies with respect to the antenna height h. In this section, we present a mean path loss model

which corresponds to the large scale fading of the channel. The envelope power of equation (1) is inversely proportional to the path loss of the channel whose averaged value is addressed by the model. In our previous paper (Fu et al., 2020), a mean path loss model has been proposed for the signal propagation inside an empty metal cavity as:

$$\overline{(\mathrm{PL})}_{dB} = \overline{(\mathrm{PL})^t}_{dB} + 10\log_{10}(|E|^2)^{-1} + 10\log_{10}([g(\alpha_t)g(\alpha_r)]^2)^{-1}, \tag{2}$$

where $\overline{(\mathrm{PL})^t}_{dB}$, $10\log_{10}(|E|^2)^{-1}$, and $10\log_{10}([g(\alpha_t)g(\alpha_r)]^2)^{-1}$ represent the traveling loss, resonant modes based power variation, and the loss due to the radiation pattern of the equipped horn, respectively. However, in this paper, we considered a more practical environment where a motherboard separates the cavity space into three parts (space below the motherboard, the motherboard, and space above the motherboard) with different dimensions as shown in Fig. 8. As compared to empty cavity, mother board desktop cavity has different resonant modes distribution. Hence, to adapt the new environment, in equation (2), we modified the factor corresponding to the resonant modes.

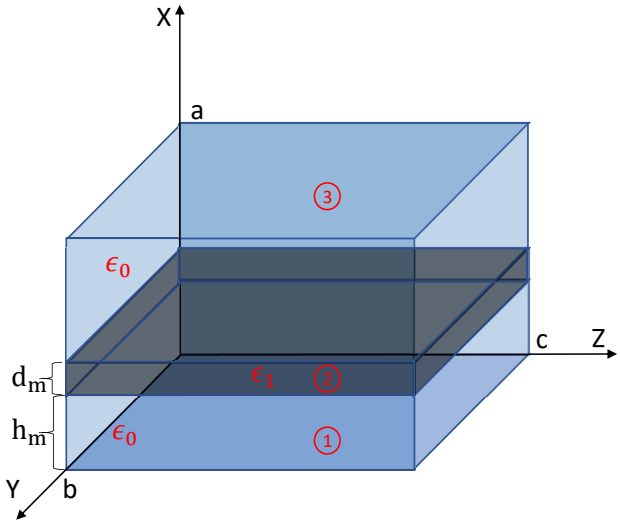

Figure 8. Simplified model for a practical desktop environment

To calculate the distribution of the resonant modes in this environment, we assumed the motherboard as a homogeneous dielectric material (FR4) and model the environment as a partially dielectric-filled resonant cavity. As shown in Fig. 8, geometry of the desktop environment is simplified as a rectangular metal cavity with the length, width, and height of c, b, and a filled by a dielectric slab with the thickness of d_m at $x = h_m$. The dielectric slab separates the cavity space into three homogeneous regions which are $0 < x < h_m$, $h_m < x < h_m + d_m$, and $h_m + d_m < x < a$. The resonant modes inside the cavity can be determined by finding the solution in each region such that tangential components of E and H fields are continuous across the common boundary.

For all the scenarios described in this paper, measurements were performed in region 3 with diagonal horn. Hence, we only cares about the E_x and E_y (TE modes) in region 3, which are calculated as

$$\begin{aligned}(E_x)_{mnp} &= \frac{-(\omega^2\mu_0\epsilon_0 - (k_{x0})_m^2)A_1}{j\omega\epsilon_0}\cos[(k_{x0})_m(a-x)]\sin\left(\frac{n\pi y}{b}\right)\sin\left(\frac{p\pi z}{c}\right)\\ (E_y)_{mnp} &= \frac{-A_1(k_{x0})_m}{j\omega\epsilon_0}\frac{n\pi}{b}\sin[(k_{x0})_m(a-x)]\cos\left(\frac{n\pi y}{b}\right)\sin\left(\frac{p\pi z}{c}\right),\end{aligned} \tag{3}$$

where ω is the radian frequency, m, n, and p are positive integers, k_{x0} is the wave number along the x direction in region 1 and 3 filled by air and can be calculated with

$$\frac{k_{x0}}{\epsilon_0}\tan\left(k_{x0}\frac{a-d_m}{2}\right) = \frac{\sqrt{k_{x0}^2+C^2}}{\epsilon_1}\cot\left(\frac{d_m\sqrt{k_{x0}^2+C^2}}{2}\right), \tag{4}$$

where $C^2 = \omega^2(\mu_1\epsilon_1 - \mu_0\epsilon_0)$, μ_0, ϵ_0, and μ_1, ϵ_1 are permittivity and permeability of air and FR4 material, respectively. Equation (4) has multiple solutions as $k_{x0} = (k_{x0})_m$. The derivations of equations (3) and (4) are shown in the Appendix Appendix A.

For the variation of antenna height h, the equation (3) can be further simplified as

$$\begin{aligned}(E_x)_m &= A_m\cos[(k_{x0})_m(a-x)]\\ (E_y)_m &= B_m\sin[(k_{x0})_m(a-x)].\end{aligned} \tag{5}$$

4.2 Gamma-Mixture Model for Shadowing across the Frequency Band

The envelope power of equation (1) fluctuates over the spectrum. This fluctuation is described as the shadowing across the frequency which also corresponds to the oscillation of the path loss over the measured frequency band. This shadowing can be treated as a random process and described by Nakagami-m distribution as it is a generalized distribution which can model different fading environments, also it has better flexibility and accuracy in matching experimental data than other models. With Nakagami fading, the corresponding instantaneous power has the gamma distribution (Stüber & Steuber, 1996):

$$\begin{aligned}f(x,m,\Omega) &= \left(\frac{m}{2\Omega}\right)^m\frac{x^{m-1}}{\Gamma(m)}\exp\left(-\frac{mx}{2\Omega}\right)\\ &= \frac{1}{\beta^\alpha\Gamma(\alpha)}x^{\alpha-1}\exp\left(-\frac{x}{\beta}\right)\\ &= f(x;\alpha,\beta),\end{aligned} \tag{6}$$

where $\alpha = m > 0$ is the shape factor, Ω is the average envelope power, $\beta = 2\Omega/m$, and $\Gamma(\cdot)$ is the Gamma function. Hence, the PDF (probability density function) of the path loss variation (corresponding to the variation of the received power with constant transmitted power) over the frequency can be modeled with Gamma distribution.

Unlike the wireless channel at low frequency, THz signal which is very sensitive and vulnerable even to the molecule in the air performs differently on different sections of the much wider frequency band. Hence, it is not sufficient to model the extremely wide band with just a single Gamma distribution (Tekbıyık et al., 2021). To fit the actual THz wireless channel, the Gamma-mixture model which covers the characteristics of each subchannel is applied.

A Gamma-mixture model consists of two types of parameters, the component weights and the component parameters (α and β) which can be derived from component means and variances. A Gamma-mixture model with L components can be expressed as (Tekbıyık et al., 2021):

$$f_G(x) = \sum_{l=1}^{L}\rho_l f_l(x,\alpha_l,\beta_l), l = 1,2,\cdots,L, x>0, \rho_l>0, \tag{7}$$

where $f_l(x,\alpha_l,\beta_l)$ follows the Gamma distribution as shown in equation (6), ρ_l denotes the mixture proportion or weight of the l^{th} component which satisfy the conditions that $0<\rho_l<1, \forall l = 1,2,\cdots,L$, and $\sum_{l=1}^{L}\rho_l = 1$.

With a given L, the EM (expectation maximization) algorithm is commonly used to determine parameters of the mixture model. EM is an iterative algorithm which has

the property that the maximum likelihood of the data strictly increase with each subsequent iteration, which means that it is guaranteed to approach a local maximum or saddle point (Brilliant.org, n.d.). The EM algorithm consists of two steps. The first step is known as the expectation (E)-step in which the membership coefficient for each data point and mixture component is computed with the expectation of component assignments for each data point given the model parameters ρ_l, α_l, and β_l. That is $\forall n, l$,

$$\phi_{n,l} = \frac{\rho_l f_l(x_n|\alpha_l, \beta_l)}{\sum_{l=1}^{L} \rho_l f_l(x_n|\alpha_l, \beta_l)}, \tag{8}$$

where $\phi_{n,l}$ is a membership coefficient, it represents the probability that the n^{th} input value x_n is generated by the l^{th} component with the the distribution $f_l(\cdot)$. The second step is the maximization (M)-step in which the calculated membership coefficients are used to update the parameters ρ_l, α_l, and β_l by maximizing the expectations calculated in E-step. That is $\forall l$,

$$\hat{\rho_l} = \frac{\sum_{n=1}^{N} \phi_{n,l}}{N}, \tag{9}$$

$$\hat{\mu_l} = \frac{\sum_{n=1}^{N} \phi_{n,l} x_n}{\sum_{n=1}^{N} \phi} = \hat{\alpha_l}\hat{\beta_l}, \tag{10}$$

$$\hat{\sigma_l^2} = \frac{\sum_{n=1}^{N} \phi_{n,l}(x_n - \hat{\mu_l})^2}{\sum_{n=1}^{N} \phi_{n,l}} = \hat{\alpha_l}\hat{\beta_l}^2, \tag{11}$$

where N is the number of input values, $\rho_l, \hat{\mu_l}, \hat{\sigma_l^2}, \hat{\alpha_l}$, and $\hat{\beta_l}$ are the updated weight, mean, variance, and scale parameters of the l^{th} component, respectively. Before the iterations, the parameters should be assigned reasonable values based on the input data through an initial step. One common way is applied here as(Brilliant.org, n.d.):

1. Randomly assign samples from the input data set $X = x_1, x_2, \cdots, x_N$ to the component mean estimates $\mu_1, \mu_2, \cdots, \mu_L$.
2. Set all component variance estimates $\sigma_1^2, \sigma_2^2, \cdots, \sigma_L^2 = \frac{1}{N}\sum_{n=1}^{N}(x_n - \bar{x})^2$, where $\bar{x}$ is the sample mean and $\bar{x} = \frac{1}{N}\sum_{n=1}^{N} x_n$.
3. Calculate α_l and β_l from the component mean and variance estimates μ_l and σ_l^2 for $l = 1, 2, \cdots L$.
4. Set all component weights to the uniform distribution $\rho_1, \rho_2, \cdots, \rho_L = \frac{1}{L}$.

4.3 Modified Saleh-Valenzuela Model For PDP

In this section, a cluster-based channel model is introduced to simulate the multipath components of THz wireless channel in a practical desktop environment. Here, cluster is defined as a group of multi-path components which have close excess delays. Clusters are always introduced from interacting with scatters (Cheng et al., 2020) such as the motherboard, components on the motherboard, and the sidewalls of the cavity. There is no standards to identify clusters. Here, the visual inspection is used by finding the local maximum and evident peaks in received power.

The introduced cluster model in this paper is a modified S-V (Saleh-Valenzuela) model. The impulse of S-V model is derived from equation (1) and given as (Meijerink & Molisch, 2014)

$$h(\tau) = \sum_{l=1}^{L}\sum_{k=1}^{K_l} g_{kl} e^{j\theta_{kl}} \delta(\tau - T_l - \tau_{kl}) = \sum_{l=1}^{L}\sum_{k=1}^{K_l} (\overline{g_{11}^2} e^{-T_l/\Gamma} e^{-\tau_{kl}/\gamma})^{\frac{1}{2}} e^{j\theta_{kl}} \delta(\tau - T_l - \tau_{kl}), \tag{12}$$

where L is the number of clusters, K_l is the number of multi-path components in the l^{th} cluster, g_{kl} and θ_{kl} are the gain and phase of the k^{th} component in the l^{th} cluster, re-

spectively. T_l is the excess delay of the l^{th} component and τ_{kl} is the delay of the k^{th} component relative to T_l. From the impulse response, the PDP of the S-V model in dB can be expressed as (Ai et al., 2015)

$$PDP(\tau) = \sum_{l=1}^{L}\sum_{k=1}^{K_l}[10\log_{10} g_{11}^2 - \underbrace{\frac{T_l}{\Gamma}(10\log_{10} e)}_{\mathrm{P}(T_l)[\mathrm{dB}]} - \underbrace{\frac{\tau_{kl}}{\gamma}(10\log_{10} e)}_{\mathrm{P}(\tau_{kl})[\mathrm{dB}]}] \cdot \delta(\tau - T_l - \tau_{kl}), \quad (13)$$

where the first term is a constant, $\mathrm{P}(T_l)$ and $\mathrm{P}(\tau_{kl})$ represent the cluster and ray decay, respectively.

The conventional S-V model is widely used, however, the assumption of S-V model on cluster and ray decay does not hold for the THz channel in desktop environment, since neither the cluster nor the ray power strictly follows the exponential decay as described in the S-V model. Hence, we proposed a modified cluster power decay as

$$\mathrm{P}(T_l)[\mathrm{dB}] = \begin{cases} c_1 \exp\left(-\frac{T_l}{d_1}\right) + e_1, \ 0 < \tau < \tau_{th1}, \\ c_2 \exp\left(-\frac{T_l}{d_2}\right) + e_2, \ \tau_{th1} < \tau < \tau_{th2}, \\ \vdots, \\ c_n \exp\left(-\frac{T_l}{d_n}\right) + e_n, \ \tau_{th(n-1)} < \tau < \tau_{Max}, \end{cases} \quad (14)$$

where $c_{1,2,\cdots n}$, $d_{1,2,\cdots n}$, and $e_{1,2,\cdots n}$ are model constants, $\tau_{th(1,2,\cdots n-1)}$ are delay thresholds severing as break points for the cluster decay $\mathrm{P}(T_l)$, and can be determined with visual inspection for different scenarios. Similarly, we modified the ray decay with power law approach as

$$\mathrm{P}(\tau_{kl})[dB] = 10n_l \log_{10}(\tau_{kl}) + \mathrm{P}_l, \quad (15)$$

where n_l is the ray decay exponent of the l^{th} cluster, and P_l is the bias. Both n_l and P_l can be determined with the least square fit to the PDP in dB for each cluster. A schematic illustration of our modified S-V model is shown in Fig. 9.

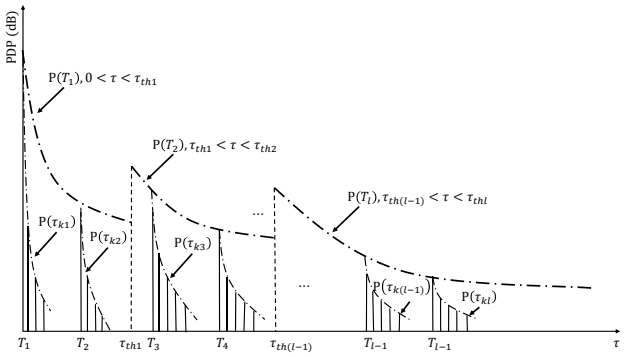

Figure 9. Schematic illustration of the proposed clustering model.

5 Result Analysis and Model Verification

In this section, we compared the path loss and PDP measured in free-space and the metal cavity for the scenarios described in section 3. Also, to model the THz channel in a practical desktop environment, we analyzed and modeled the motherboard desktop measured path loss with proposed mean path loss model and Gamma-mixture model

for the shadowing of the path loss across the frequency, and measured PDP with the modified S-V model. For the Gamma-mixture model applied in each scenario, the number of mixed Gamma distributions, k, is chosen to achieve more than 97% of r-squared goodness of fit. Also, the parameters of cluster and ray power decay in modified S-V model are summarized in tables.

5.1 Path Loss and Multipath Characterization

the calculations of path loss and PDP from the measured data for the scenarios described in Section 3 are introduced here. Path loss refers to the power drop of the EM wave as it propagates through a wireless channel. The measured path loss PL, here, is represented as:

$$\mathrm{PL} = \frac{P_t G_t G_r}{P_r}, \tag{16}$$

where P_t, P_r, G_t and G_r are refer to the transmitted power, received power, transmit gain, and receive gain, respectively. With the S21 (P_r/P_t) collected by the VNA and the known antenna gain, the measured path loss PL can be easily calculated. The measured path loss is compared with the theoretical free-space path loss $\tilde{\mathrm{PL}}$ defined as:

$$\tilde{\mathrm{PL}} = (\frac{4\pi d}{\lambda})^2, \tag{17}$$

where d and λ represent the signal traveling distance and the wave length in free space, respectively.

PDP provides the intensity of a signal received through a multipath channel as a function of time delay. Also, some other important parameters such as mean excess delay, RMS delay spread, and coherence bandwidth are calculated from the PDP. The measured PDP file can be derived by squaring the normalized channel impulse response which can be estimated through inverse discrete Fourier transform (IDFT) of the measured frequency response.

5.2 Characterization and Modeling of LoS Propagation

Section 3.1, Fig. 3 describes the measurement scenario for LoS link over the motherboard in free-space and the metal case. Figure 10 compares the measured and Friis predicted path loss for antenna height varies from 0 to 2.4 cm with the step of 0.6 cm. As shown in Fig. 10a and Fig. 10b, a similar trend of the path loss variation w.r.t. the antenna height can be observed in both free-space and desktop metal cavity scenarios. We observe destructive effects when $h = 0$ cm, and 1.2 cm with the measured path loss of 3 dB and 2 dB greater than Friis predicted value, respectively, for both scenarios. In contrast, when antenna height is 0.6 cm, the interference with the reflection on the motherboard and the effect of resonant modes inside the cavity provide constructive effects to the wireless channel, which results in the path loss measured in free-space and motherboard desktop to be 2 and 2.5 dB lower than the Friis value, respectively. And when h is greater or equal to 1.8 cm, the measured path loss follows the Friis line very well in both scenarios.

Figure 11 compares the measured and theoretical mean path loss w.r.t. the heights of transceivers. Please note that x represents the distance between the phase center of antennas and the bottom of the cavity, which is the antenna height, h, being biased with a constant. The mean path loss at a certain height is calculated by averaging the continuous wave over all recorded frequencies as

$$\overline{\mathrm{PL}} = \frac{1}{N}\sum_{i=1}^{N} \mathrm{PL}(f_i), \tag{18}$$

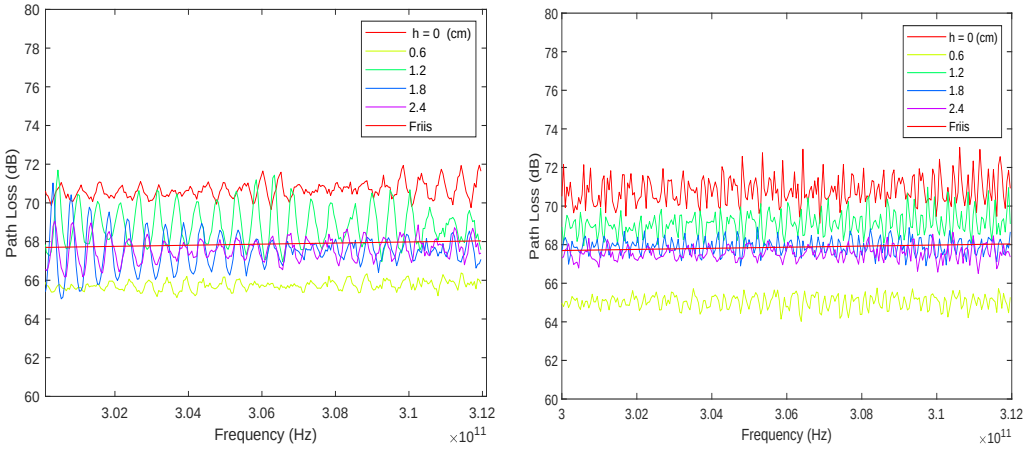

Figure 10. Measured and theoretical path loss curves for LoS link (a) in free-space (b) inside the metal cavity with antenna over the motherboard varies from 0 cm to 2.4 cm.

where N=801 is the number of sampled points over the frequency band. The theoretical path loss is calculated with equation (2), where $\overline{(\mathrm{PL})^t}$ is the traveling loss which can be calculated by averaging the Friis equation over the measured frequency band and is equal to 67.87 dB for the LoS link. The term $10\log_{10}(|E|^2)^{-1}$ represents the resonant based power variation with

$$|E|^2 = |E_x|^2 + |E_y|^2 = |\sum_{m=1}^{M} E_{xm}|^2 + |\sum_{m=1}^{M} E_{ym}|^2, \tag{19}$$

where E_{xm} and E_{ym} can be derived from (5) with the cavity height $a = 10$ cm, and the wave number in x-direction k_{x0} can be determined using (4), where $d_m = 1.6$ mm, $\epsilon_1 = 4.4\epsilon_0$, and $\mu_1 \approx \mu_0$. It is calculated that $(k_{x0})_m \approx 0.3196 + \frac{m\pi}{4.92}$, $m \in N^+$. During the measurements, both Tx and Rx were moved simultaneously, hence, the last term corresponding to the loss due to the radiation pattern is negligible. It can be observed that the path loss predicted by the model matches well with the measured results except the point when antennas are on the motherboard. This is because in our model, motherboard is treated as a homogeneous dielectric slab and the desktop environment is modeled as a partially dielectric-filled resonant cavity which is an abstract of the practical environment. It is found that the first sixteen TE modes ($M = 16$) dominate the channel. The coefficients, A_m and B_m for each mode were found by curve-fitting the interpolated measured mean path loss.

The oscillations of path loss measured in free-space are due to the reflections on the motherboard and between the back-panels of both Tx and Rx antennas. On comparison, it is observed that the motherboard desktop measured path loss varies more rapidly and randomly, which may due to the resonant modes in cavity (Fu et al., 2019b; Fu et al., 2020). To characterize the shadowing across the frequency as path loss variation over the band, the gamma mixture model as described in section 4.2 is applied. Figure 12 shows that Gamma-mixture model described by equation (7) has good fit to the PDF of in-cavity measured path loss oscillations with antenna height $h = 0.3,\ 1.5,\ 2.4,\ 3.3$, and 4.5 cm, and the corresponding number of mixed Gamma distributions, k, are chosen to be 6, 6, 6, 14, and 13, respectively, to achieve the r-squared goodness of fit to be greater than 97%. Also, it is observed that by increasing the number of Gamma distributions in the mixture, fitting to the measurements can reach a higher accuracy.

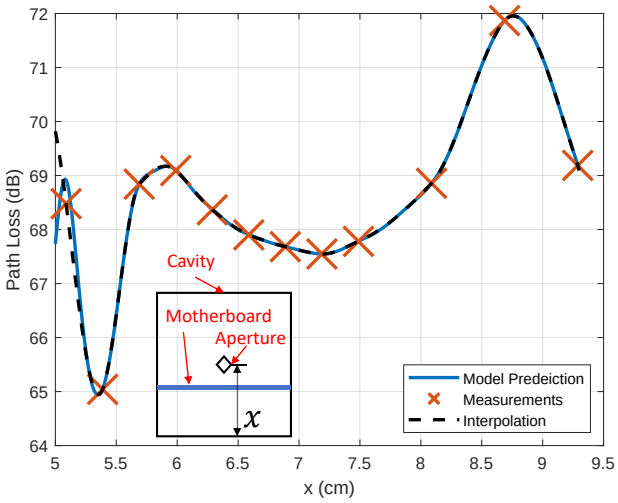

Figure 11. Comparison of theoretical and measured path loss with respect to the transceiver's height for THz LoS link inside metal cavity.

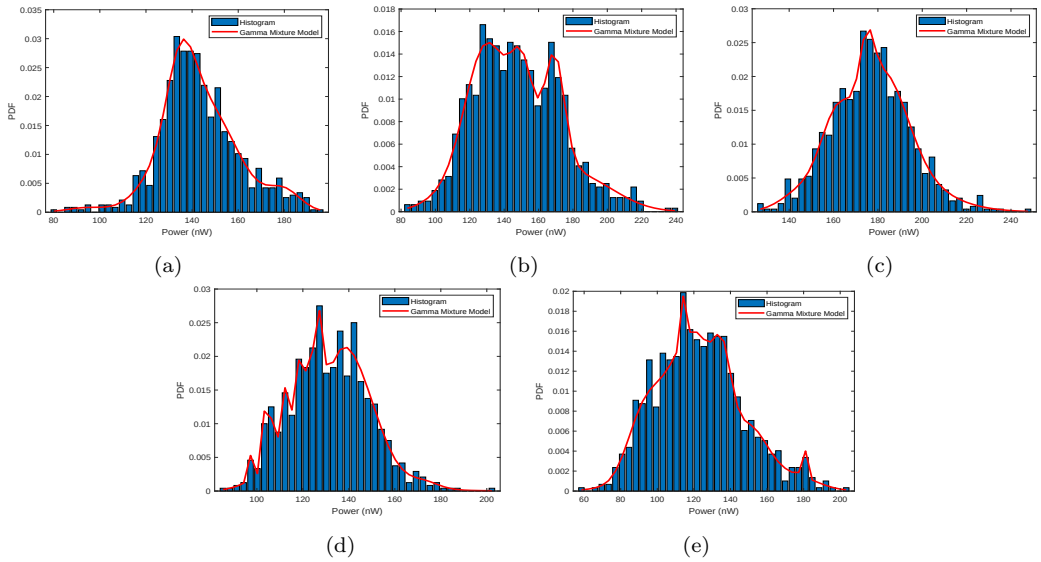

Figure 12. Gamma-mixture model for the PDFs of motherboard desktop measured path loss variation for LoS link with: (a) $h = 0.3$ cm, $k = 6$, R-squared: 97.3795%, (b) $h = 1.5$ cm, $k = 6$, R-squared: 97.6825%, (c) $h = 2.4$ cm, $k = 6$, R-squared: 97.787%, (d) $h = 3.3$ cm, $k = 14$, R-squared: 97.4036%, and (e) $h = 4.5$ cm, $k = 13$, R-squared: 97.4965%.

Figure 13 presents the PDP files measured in free-space and motherboard desktop with five different antenna heights h from 0 to 2.4 cm. For the PDP file measured in free-space, as shown in Fig. 13a, there are two clusters of later arriving peaks with excess delay of 1.918 and 3.92 ns from which the extra distances covered by the signal are calculated. And the calculated distances are exactly two and four times of the spacing between the back panels of antennas, which means that these two groups of later arriving peaks are due to the signal bouncing back and forth between the back panels of the antennas. Inside the metal cavity, more multipaths can be observed, as shown in Fig. 13b, the PDP measured inside the metal cavity has five periodic clusters of later arriving peaks with

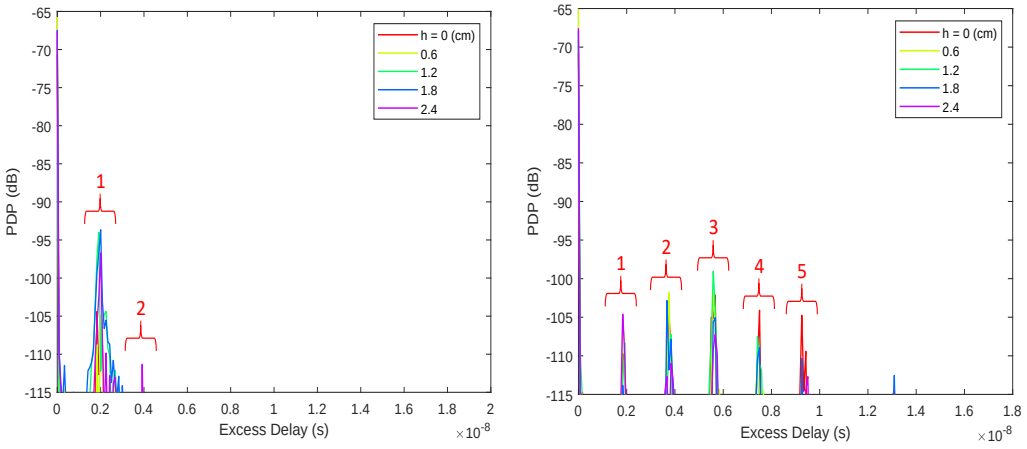

(a) (b)

Figure 13. Measured PDP files for LoS link (a) in free-space (b) inside the metal cavity with antenna over the motherboard varies from 0 cm to 2.4 cm.

the period of 1.835 ns, which indicates that the signal inside the cavity bouncing back and forth between the transceiver sidewalls (side A and C) of the cavity.

To characterize the THz wireless link in such practical desktop environment comprehensively, all local PDPs are first linearly averaged to generate the averaged power delay profile APDP(τ) as

$$\text{APDP}(\tau) = E[\text{PDP}(\tau, h)], \tag{20}$$

where $E[\cdot]$ represents the ensemble average on all PDP files measured with different antenna heights. The modified S-V model as described in section 4.3 is adopted to characterize the APDP of the THz LoS link in the practical desktop environment. It can be observed from Fig. 14 that there is a good match between the measured and modeled results. From the plot, it can be easily identified that there are ten clusters with visual inspection. The cluster power decay can be modeled with equation (14) with two sub-functions ($n = 2$). The model coefficients for the cluster power decay are summarized in Table. 2. The ray power decay in each cluster can be modeled with equation (15), the

Table 2. Parameters of cluster power decay for LoS link in a desktop environment

n	c	d	e
1	-42.34	0.735	42.34
2	-64.28	0.945	64.47

ray decay exponent n_l and bias P_l are summarized in Table. 3.

5.3 Characterization and Modeling of RNLoS Propagation

Figure 15 compares the path loss of RLoS link measured in both free-space and the metal cavity with the Friis prediction. Measurement setup is described in section 3.2 and shown in Fig.4.Measured path loss curves with both component side and flat side of the

Table 3. Parameters of cluster power decay for LoS link in a desktop environment

l	n_l	P_l
1	1.1160	58.4137
2	1.0052	20.0044
3	1.3832	16.7649
4	1.4564	24.6808
5	1.4134	19.2755
6	0.9636	14.6103
7	0.9407	12.0981
8	0.6336	9.8471
9	0.3687	7.2212
10	0.3662	5.3088
11	0.0714	4.2113

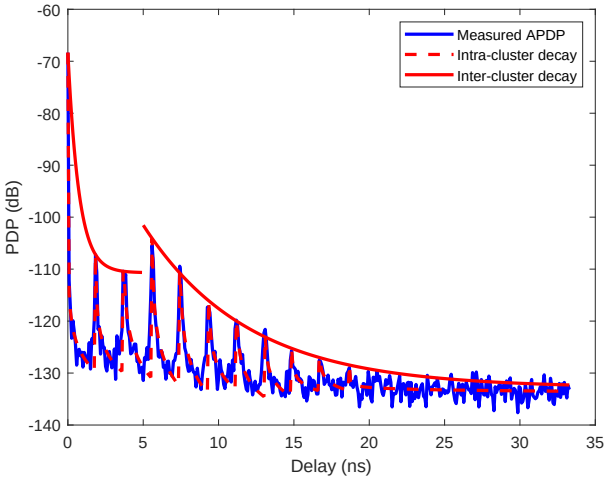

Figure 14. Comparison of measured and modeled APDPs for THz LoS link in a practical desktop environment.

DIMM as reflecting surface are compared. As shown in the plot, the path losses for both component and flat side of the DIMM are greater than the Friis prediction, which is due to the reflection losses. Also, since the component side is more rugged than the flat side of the DIMM, the path loss measured on the component side of the DIMM is greater than which measured on the flat side. Considering the effects of resonant modes inside the cavity, the path loss measured inside the cavity is about 1 dB lower than the path loss measured in free-space with flat side of the DIMM as the reflection surface. Since the oscillation of path loss over the measured frequency band is mainly due to the multipath

introduced by the scatterings on the DIMM and the resonant modes inside the cavity. The fluctuation of the path loss measured on the component side and inside the metal cavity is stronger than which measured on the flat side and in free-space.

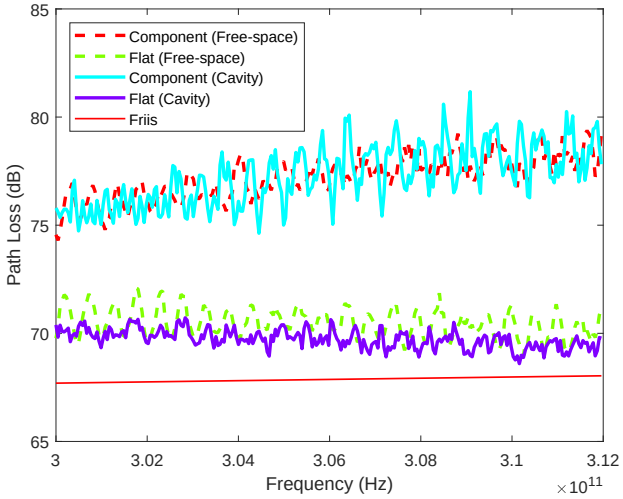

Figure 15. Measured and Friis predicted path loss curves for RNLoS link with measurements performed on component and flat side of the DIMM and in both free-space and metal cavity.

The oscillation of path loss measured inside the metal cavity is characterized by the described Gamma-mixture model as shown in Fig. 16. A good match between the Gamma-mixture models described by equation (7) and the PDFs of the in-cavity measured path loss oscillations with component side and flat side as the reflection surface. The corresponding number of mixed distributions, k, are chosen to be 12 and 6, respectively.

Figure 17 shows the PDP files measured in free-space and the metal cavity with both component side and flat side of the DIMM as the reflection surfaces. As shown in the plot, for the PDP files measured in free-space, there are two clusters of later arriving peaks with excess delay of 1.01 and 1.918 ns which are due to the signal propagating to the Rx through the reflection on the DIMM with an extra traveling between the DIMM and the back-panel of Tx or Rx and an extra traveling between the back-panels of Tx and Rx, respectively. For the PDP files measured inside the metal cavity, more multipaths can be observed as there are four clusters of later arriving peaks. The first cluster of later arriving peaks with the excess delay of 0.83 ns indicates an extra traveling of the signal between the DIMM and a transceiver sidewall (sidewall A or D) of the cavity. Other three later arriving peaks with the period of 1.83 ns are due to the signal bouncing back and forth between the transceiver sidewalls.

To model the PDP of THz RNLoS link with DIMM as the reflector, the APDP file is first calculated by averaging the PDP files measured with both sides of the DIMM. The modified S-V model is applied to characterize the calculated APDP file. As shown in Fig. 18, a good match between modeled and measured results can be observed. With the visual inspection, thirteen clusters can be identified from the plot. The cluster power decay is modeled by equation (14) with four sub-functions ($n = 4$). The values of model coefficients for the cluster power decay is summarized in Table. 4. In each cluster, the ray power decay is described by the equation (15), the ray decay exponent n_l and bias P_l are summarized in Table. 5.

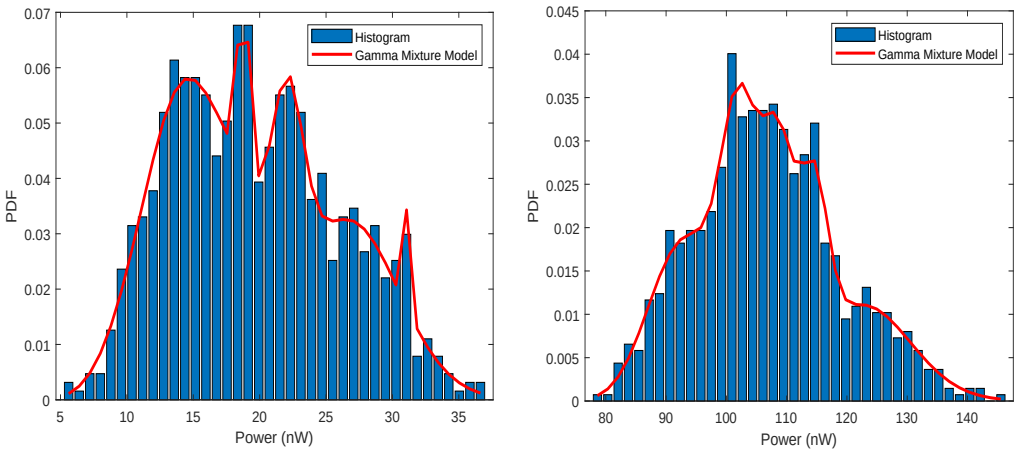

(a) (b)

Figure 16. Gamma-mixture model for the PDFs of motherboard desktop measured path loss oscillations for RNLoS link with (a) component side as the reflection surface, k = 12, R-squared: 97.4036% (b) flat side as the reflection surface, k = 6, R-squared: 97.7893%.

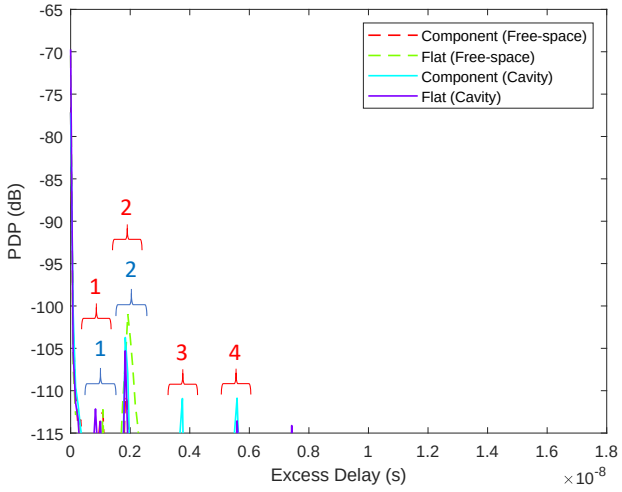

Figure 17. Measured PDP files for RNLoS link with measurements performed on component and flat side of the DIMM and in both free-space and metal cavity.

Table 4. Parameters of cluster power decay for RNLoS link in a desktop environment

n	c	d	e
1	-51.29	0.6298	51.29
2	-83.87	12.06	103.1
3	-64.65	6.544	66.3
4	-52.78	4.225	52.77

Table 5. Parameters of cluster power decay for RNLoS link in a desktop environment

l	n_l	P_l
1	2.2146	53.7255
2	0.3717	13.5386
3	0.5510	22.0297
4	0.2120	11.5867
5	0.9899	13.4107
6	0.2684	15.0330
7	0.9600	15.9388
8	0.9132	13.5593
9	0.7131	11.3728
10	0.2922	9.0637
11	-0.0658	8.7841
12	0.3539	8.2470
13	-0.2434	8.9768

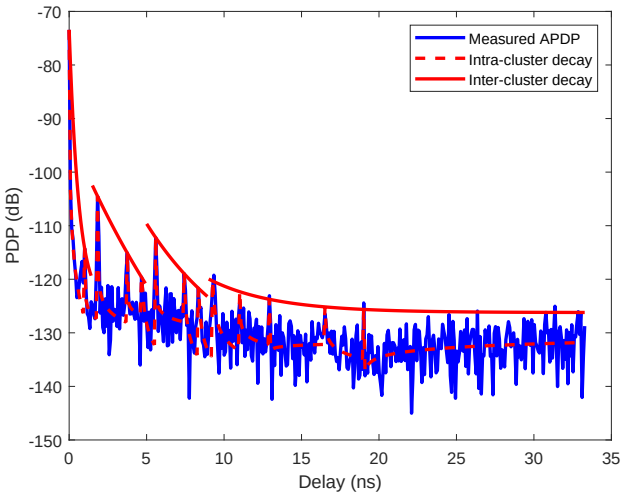

Figure 18. Comparison of measured and modeled APDPs fro THz RNLoS link in a practical desktop environment.

5.4 Characterization and Modeling of OLoS Propagation

The measurement setup for the characterization of OLoS propagation over the motherboard in free-space and metal desktop case is described in Section 3.3 and shown in Fig. 5. A similar trend on the transition of path loss measured in free-space and inside

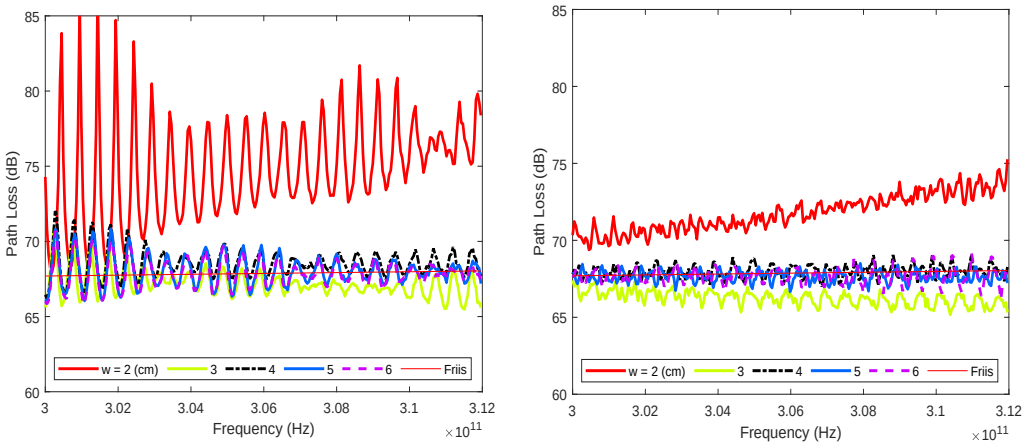

Figure 19. Measured and theoretical path loss curves for OLoS link (a) in free-space (b) inside the metal cavity with the distance between parallel DIMMs varies from 2 cm to 6 cm.

the metal cavity w.r.t. the variation of distance between the parallel DIMMs, w, can be observed from Fig. 19a and Fig. 19b. Comparing with the Friis prediction, destructive and constructive effects can be seen when $w = 2$ and 3 cm, respectively. The destructive and constructive effects indicates the scattering and multipaths inside the corridor created by the parallel DIMMs. And the these effects die out when $w \geq 4$ cm where path loss follows the Friis prediction very well. The differences between the path loss curves measured in free-space and inside the metal cavity are also very obvious. As shown in the plots, the path loss curves measured in free-space when $w = 2$ and 3 cm are greater than which measured inside the metal cavity. Also, the oscillations of the path loss curves measured in free-space are stronger in terms of the amplitude, while the path loss measured inside the cavity varies more rapidly and randomly over the measured band. These oscillations are due to the multipath introduced by the scatterings between the Parallel DIMMs, the reflections on the motherboard, and reflections between back-panels of equipped antennas for path loss measured in free-space, and resonant modes for path loss measured inside the metal cavity.

The Gamma-mixture model described in section 4.2 is applied to characterize the oscillations of path losses measured in the practical desktop environment. As shown in Fig 21, a great agreement between the Gamma-mixture model described by equation (7) and the PDFs of oscillations of path losses measured with $w = 3$ and 5 cm. The corresponding number of Gamma-distributions applied for each channel response, k, are chosen to be 8 and 20.

The PDP files of OLoS link measured in free-space and inside the metal cavity with distance between DIMMs $w = 2, 3, 4, 5$, and 6 cm are shown in Fig. 21. For the PDP files measured in free-space, as shown in Fig. 13a, there are three clusters of later arriving peaks with the delay of 1.918, 3.92, and 6 ns, which are due to the signal bouncing between the back-panels of the equipped antennas while for the PDP files measured inside the metal cavity shown in Fig. 21b, five periodic clusters of later peaks with the 1.83 ns period can be observed, which are due to the signal bouncing back and forth between the transceiver sidewalls of the cavity.

The averaged power delay profile APDP for the OLoS link inside the practical desktop is first calculated by averaging the local PDPs measured with different distances be-

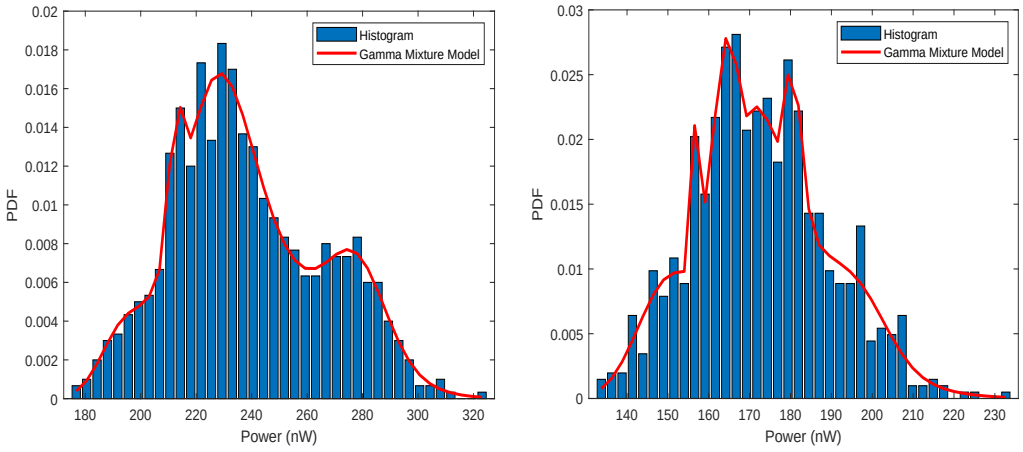

(a) (b)

Figure 20. Gamma-mixture model for the PDFs of motherboard desktop measured path loss oscillations for OLoS link with the distance between the parallel DIMMs (a) $w = 3$ cm, k = 8, R-squared: 97.6146% (b) $w = 5$ cm, k = 20, R-squared: 97.1241%.

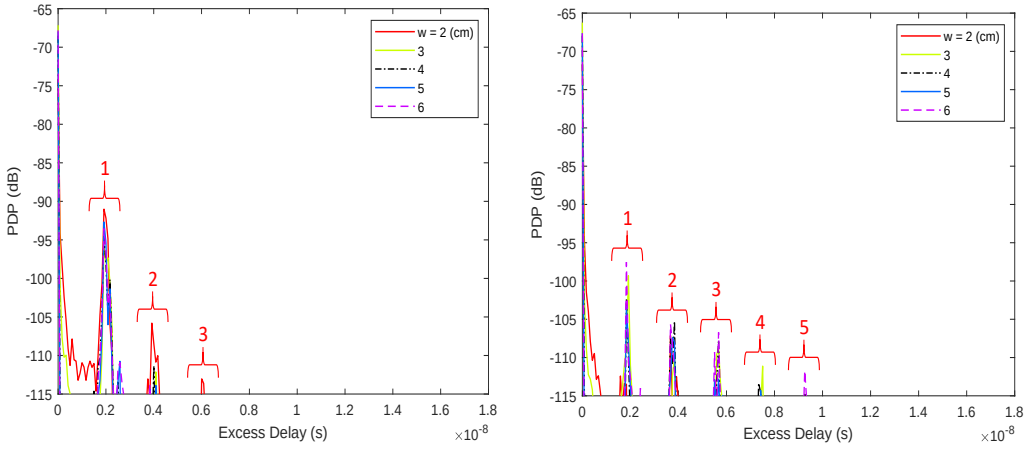

(a) (b)

Figure 21. Measured PDP files for OLoS link (a) in free-space (b) inside the metal cavity with distance between the parallel DIMMs varying from 2 cm to 6 cm.

tween the parallel DIMMs. The modified S-V model is used to characterize the calculated APDP file. As shown in Fig. 22, a good agreement between the Gamma-mixture model and the measured result can be observed. Ten clusters can be identified with the visual inspection from the plot. The cluster power decay can be described with equation (14) with two sub-functions (n = 2). The parameter values are summarized in Table. 6 for the cluster power decay. Also, the ray power decay can be described with the

Table 6. Parameters of cluster power decay for OLoS link in a desktop environment

n	c	d	e
1	-43.38	0.9769	43.39
2	-60.2	4.949	60.22

equation (15), the ray decay exponent n_l and the bias P_l are summarized in Table. 7.

Table 7. Parameters of cluster power decay for OLoS link in a desktop environment

l	n_l	P_l
1	1.0456	57.2337
2	1.0749	20.7884
3	1.4130	16.4080
4	1.4096	17.3007
5	1.1173	15.8399
6	0.9047	11.3656
7	0.5777	9.5487
8	0.3258	8.6060
9	0.4507	8.2769
10	0.1474	6.0833

5.5 Characterization and Modeling of NLoS Propagation

NLoS propagation measurements has been performed on the motherboard with heat sink as the obstruction in both free-space and metal cavity as described in section 3.4 and the measurement setup is shown in Fig. 6. Figure 23 compares the measured path loss with different horizontal movements of the heat sink, y, with the Friis prediction. The destructive effects of the heat sink can be clearly observed from the plot. For the path loss measured in free-space as shown in Fig. 23a, all measured curves oscillate around 80 dB which is about 12 dB greater than the Friis prediction. And for the in-cavity mea-

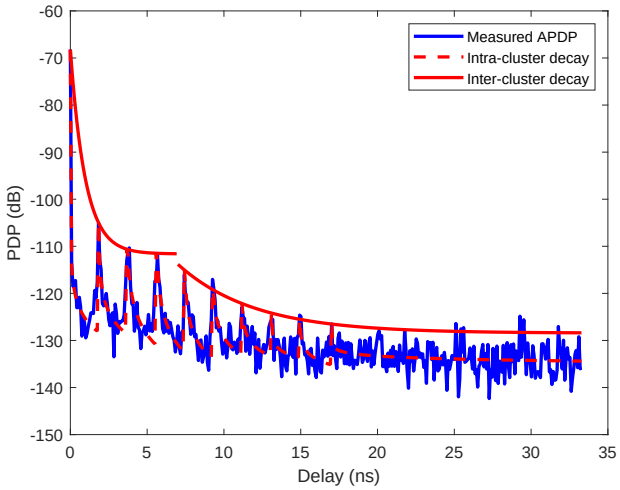

Figure 22. Comparison of measured and modeled APDPs for THz OLoS link in a desktop environment.

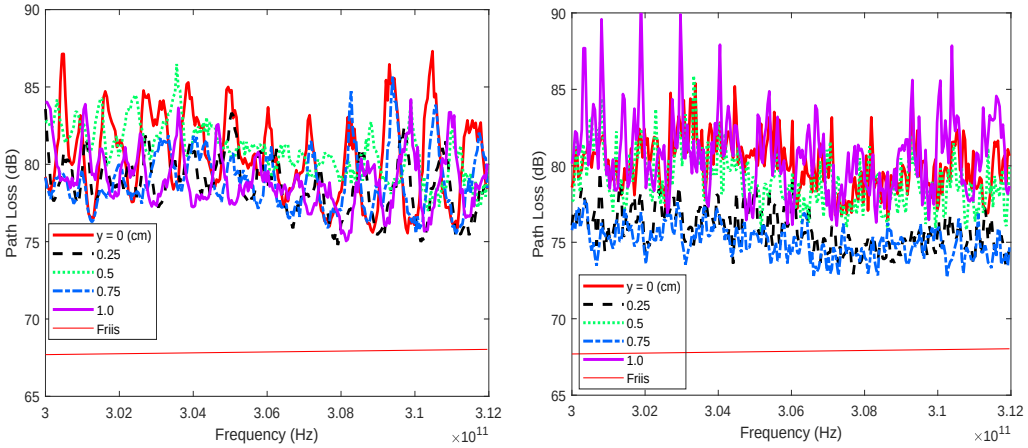

(a) (b)

Figure 23. Measured and theoretical path loss curves for NLoS link (a) in free-space (b) inside the metal cavity with horizontal movement of the heat sink from 0 to 1 cm.

surements as shown in Fig. 23b, the path loss curves measured with $y = 0.25$ and 0.75 cm are around 75 dB, while other three curves are around 80 dB. Also, due to the scatterings on the fins of the heat sink, and the reflections on the motherboard, strong oscillations of the path loss curves can be observed from both Fig. 21a and Fig. 21b. However, due to the resonant modes inside the metal cavity, the in-cavity measured path loss varies more rapidly and oscillates more strongly for some certain values of y.

The oscillations of the path losses measured inside the metal cavity can be described by the mixture of several Gamma distributions as mentioned in section 4.2. Figure 24 compares the PDFs of the Gamma-mixture model described by equation (7) and the path loss measured with $y = 0.5$ and 1 cm. The number of mixed Gamma-distributions for each channel response, k, are chosen to be 15 and 9.

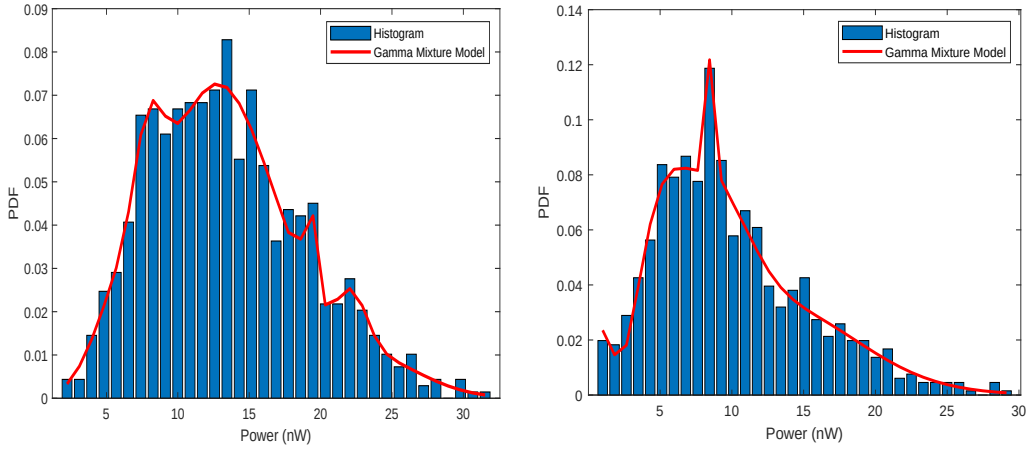

Figure 24. Gamma-mixture model for the PDFs of motherboard desktop measured path loss oscillations for NLoS link with horizontal movements of the heat sink (a) $y = 0.5$ cm, k = 15, R-squared: 97.1670% (b) $w = 1$ cm, k = 9, R-squared: 97.3274%.

The PDP files of NLoS propagation measured in free-space and inside the metal cavity with different horizontal movements of the heat sink as the obstacle are shown in Fig. 25a and Fig. 25b, respectively. For the PDP files measured in free-space, there are three clusters of later arriving peaks with the excess delay of 0.9174, 1.918, and 2.585 ns. The first and second cluster of later arriving peaks are due to the extra traveling of the signal between fins of the heat sink and the back panel of Tx or Rx, and extra traveling between the back panels of equipped antennas, respectively. And the third cluster of later arriving peaks indicates that the signal not only traveled an extra distance between the back panels of equipped antennas, but also an extra distance between the fins and the back panel of the Tx or Rx antenna. For the PDP files measured inside the metal cavity, there are seven clusters of later arriving peaks. The second, fourth, and sixth cluster of later arriving peaks with the excess delay of 1.835, 3.837, and 5.671 ns (1, 2, and 3 $\times$1.835 cm) are due to the signal bouncing back and forth between the transceiver sidewall of the cavity. And the first, third, fifth, and seventh cluster of later arriving peaks with the excess delay of 0.834, 2.669, 4.587, and 6.422 ns indicate that besides rebounding between the transceiver sidewalls of the cavity, signal also bounces around the transceiver sidewall (A or C) and fins of the heat sink.

The APDP file for the NLoS link inside the cavity is first calculated by averaging all local PDPs measured with different horizontal movements of the heat sink. The calculated APDP is then characterized by the modified S-V model. As shown in Fig. 26, a good match between the modified S-V model and the APDP can be observed. From the plot, 16 clusters can be identified with visual inspection. The cluster power decay can be modeled with equation (14) with three sub-functions (n = 3). The break points τ_{th1} and τ_{th2} are 4, and 13 ns, respectively. The model coefficients of the cluster power decay are summarized in Table. 8. Also, the ray power decay in each cluster can be described with equation (15). The ray decay exponent n_l and the bias P_l are summarized in Table. 9.

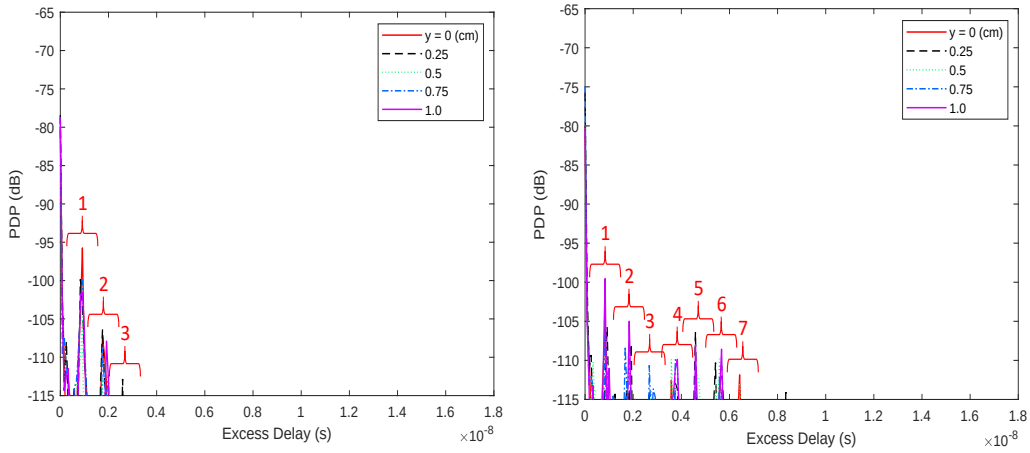

(a) (b)

Figure 25. Measured PDP files for NLoS link (a) in free-space (b) inside the metal cavity with horizontal movements of the heat sink varying from 0 cm to 1 cm.

Table 8. Parameters of cluster power decay for NLoS link in a desktop environment

n	c	d	e
1	-37.22	0.6561	37.29
2	-54.04	5.073	54.04
3	-5.467×10^7	0.8058	51.9292

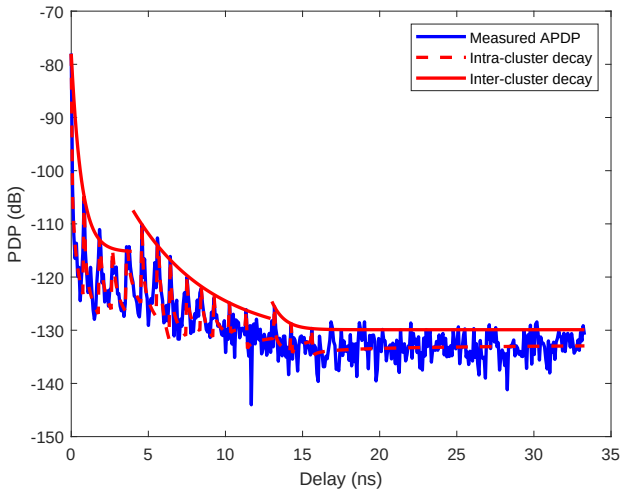

Figure 26. Comparison of measured and modeled APDPs for THz NLoS link in a desktop environment.

5.6 Characterization and Modeling of CPU-PCI Link

On the densely populated motherboard, CPU-PCI connection is a commonly used link. Measurements of the CPU-PCI link were performed as described in section 3.5 and

Table 9. Parameters of cluster power decay for NLoS link in a desktop environment

l	n_l	P_l
1	1.9499	47.5852
2	1.0973	22.4998
3	1.0685	14.3989
4	0.9128	12.4622
5	0.9326	10.0692
6	0.8716	17.6068
7	1.7561	19.7556
8	0.7303	14.2553
9	0.5127	10.7850
10	0.6559	10.3208
11	0.3066	7.2974
12	-0.0680	4.8463
13	-0.1428	5.6486
14	0.2937	8.4393
15	-0.1786	3.5601
16	-0.0794	4.2471

the setup is shown in Fig. 7. Figure 27 compares the path loss measured in free-space and the metal cavity with different distances between the transceivers with the corresponding Friis predictions. For the path loss measured in Free-space, as shown in Fig. 27a, all measured path loss curves are around 86 dB which is about 20 dB greater than the Friis predictions. No clear hierarchy can be observed from the measured path loss even though the T-R separation was gradually increased with the step of 1 cm. The high path loss is due to the obstruction of components on the mother board like the heat sink and the 3 cm vertical misalignment between the Tx and Rx. Because of the scatterings on the densely populated motherboard and the reflections between the back-panels of the antennas, strong ripples with the maximum of ∼15 dB can be observed on the measured path loss curves. For the in-cavity measurements, the measured path losses still oscillates around approximate 86 dB as shown in Fig. 27b. However, different with the path loss measured in free-space, the in-cavity measured path loss oscillates more randomly and rapidly due to the resonant modes inside the cavity.

Oscillations of the in-cavity measured path losses are considered as random processes and modeled by the described Gamma-mixture model. Figure 28a and 28b compare the PDFs of the Gamma-mixture model described by equation (7) and the path loss measured with the T-R separation, $d = 20.3$ and 22.3 cm, respectively. The number

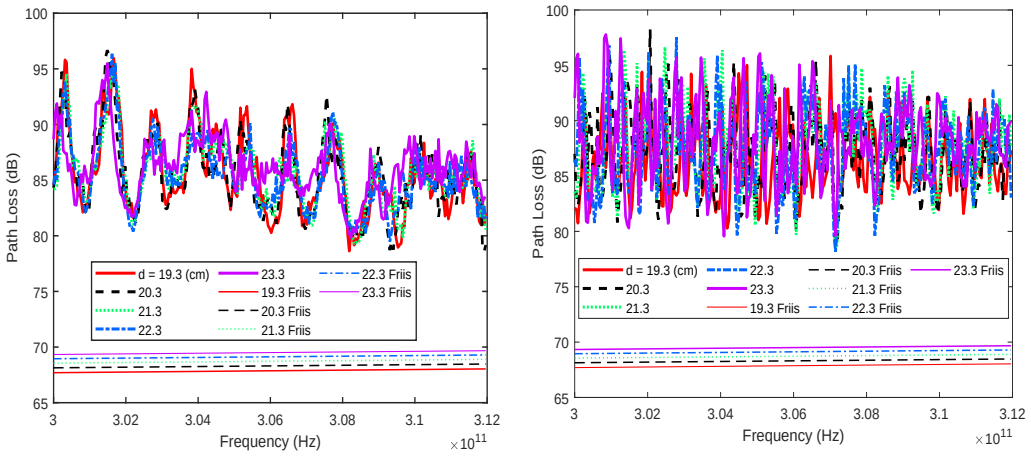

Figure 27. Measured and theoretical path loss curves for CPU-PCI link (a) in free-space (b) inside the metal cavity with the T-R separation varying from 19.3 cm to 23.3 cm, while keeping the height difference to be 3 cm.

of mixed distributions for each channel response, k, are chosen to be 6 and 2, respectively.

Figure 29a shows the PDP files measured in free-space with T-R separation $d =$ 19.3, 21.3, and 23.3 cm. Considering the number of multipaths introduced by the scatterings on the densely populated motherboard, the measured PDP are disordered. However, it can be observed from the plot that all these PDP files shared two clusters of later arriving peaks with the excess delay of 0.334 ns and 0.834 ns, which indicates the extra traveling of the signal between the heat sink and the accelerated graphics port (the green socket as shown in Fig. 7) and between the heat sink and the back-panel of the Tx antenna, respectively. Figure 29b shows the in-cavity measured PDPs. Seven clusters of later arriving peaks can be observed from the plot. The second, fourth, and sixed cluster of later arriving peaks with the excess delay of 1.835, 3.67, and 5.588 ns are due to the signal bouncing back and forth between the transceiver sidewalls of the cavity. The first, third, fifth, and seventh cluster of later arriving peaks with the excess delay of 0.75, 2.669, 0.4504, and 6.339 ns suggest that besides the bouncing between the transceiver sidewalls, signal also bounces between the heat sink and the Tx sidewall.

To model the CPU-PCI link on the motherboard inside the desktop case, the APDP file is first calculated by averaging the local PDPs with different T-R separations. Fig. 30 compares the calculated APDP file and the modified S-V model. As shown in the plot, a good match between the measured and modeled results can be observed. Ten clusters can be easily identified from the plot with visual inspection. Equation (14) models the cluster power decay with four sub-functions, and the break points τ_{th1}, τ_{th2}, and τ_{th3} are 2.2, 4.2, and 6 ns. Table. 10 summarizes the coefficients of the cluster decay. Inside each cluster, the ray power decay can be modeled with equation (15). The decay exponent n_l and bias P_l for each cluster are summarized in Table. 11.

6 Conclusions

This paper presented the THz channel characterization and modeling for a practical desktop environment. Measurements were performed on a motherboard both in free-

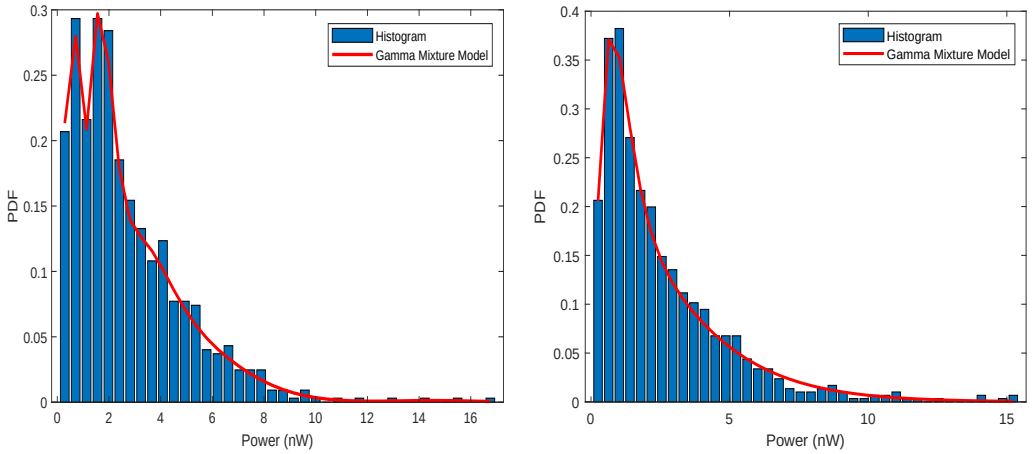

(a) (b)

Figure 28. Gamma-mixture model for the PDFs of in-cavity measured path loss oscillations for CPU-PCI link with T-R separation (a) d = 20.3 cm, k = 6, R-squared: 99.3121% (b) d = 22.3 cm, k = 2, R-squared: 99.2881%.

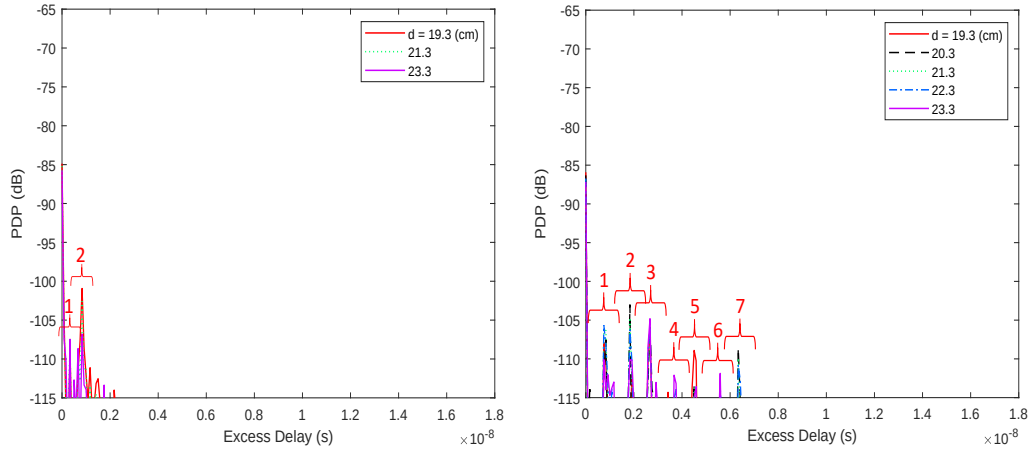

(a) (b)

Figure 29. Measured PDP files for CPU-PCI link (a) in free-space (b) inside the metal cavity with the T-R separation varying from 19.3 cm to 23.3 cm, while keeping the height difference to be 3 cm.

Table 10. Parameters of cluster power decay for CPU-PCI link in a desktop environment

n	c	d	e
1	-22.4	0.2013	22.4
2	-105.7	2.165	50.1
3	-44.04	3.719	40.2
4	-106.7	3.261	42.2

Table 11. Parameters of cluster power decay for CPU-PCI link in a desktop environment

l	n_l	P_l
1	0.1954	35.9348
2	1.6014	18.8449
3	1.4081	22.0788
4	1.7885	27.9377
5	1.1900	14.7129
6	1.1396	17.4574
7	1.4631	20.9202
8	0.9116	17.0405
9	0.4252	11.5354
10	0.3102	9.4628

space and inside a desktop size metal cavity with the consideration of several potential scenarios. Path loss and PDPs measured in different environments are compared. The results show that mean path loss measured inside the motherboard desktop changes in the same manner as which measured in free-space. However, the path loss measured inside the motherboard desktop oscillates more rapidly and randomly due to the resonant modes inside the cavity. Also, because of the resonant modes, more multipath components can be observed from the in-cavity measured PDP plots. The periodic clusters of later arriving peaks with 1.835 ns period indicate the signal bouncing back and forth between the transceiver sidewalls. The large scaling fading of the path loss can be characterized with our mean path loss model as a function of antenna height, h. The model expression is derived by simplifying the environment as a partially dielectric filled metal cavity. The modified mean path loss model has a good agreement with the measured mean path loss except the first point where antennas were on the motherboard. Considering the ultra-wide bandwidth and rapid changes of the signal at THz frequency, Gamma-mixture model is applied to characterize the random process of the oscillations of in-cavity measured path loss. Results show that with proper choice of the number of mixed Gamma distributions k, the goodness of fit between the model and the PDF of path loss oscillations can reach more than 97%. Also, with larger k, the accuracy can be better. Mul-

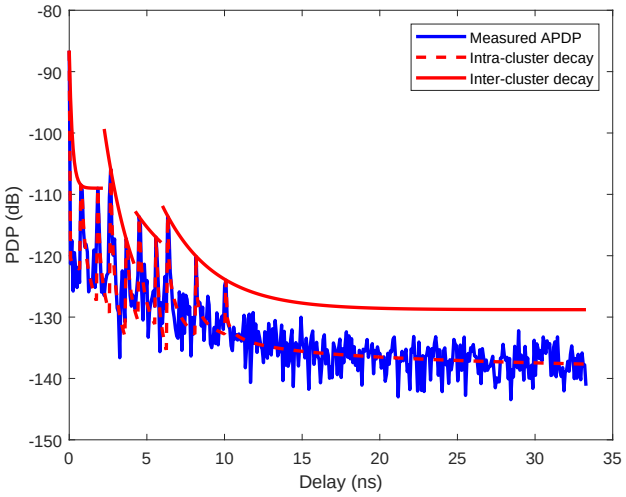

Figure 30. Comparison of measured and modeled APDPs for CPU-PCI link in a practical desktop environment.

tipath components are characterized by cluster-based channel modeling. To better fit the measured results, modifications were made on the conventional S-V model by expressing the cluster power decay with step-wise functions and each sub-function is expressed exponentially in dB, and the ray power decay with power law approach. A good match between the model and the measurements was observed, which verifies the correctness of our modified S-V model.

Appendix A Derivation of Resonant Modes Distribution in a Practical Desktop Environment

Here, we attempt to find the TM to x modes in the cavity. The field equations in homogeneous regions can be constructed through the general solutions to the scalar Helmholtz equation which is (Harrington, 2001)

$$\frac{\partial^2\psi}{\partial x^2}+\frac{\partial^2\psi}{\partial y^2}+\frac{\partial^2\psi}{\partial z^2}+k^2\psi=0. \tag{A1}$$

The general solution to the Helmholtz equation is (Harrington, 2001)

$$\psi_{k_xk_yk_z}=f(k_xx)f(k_yy)f(k_zz), \tag{A2}$$

where the parameters satisfy $k_x^2+k_y^2+k_z^2=k^2$ and $f(k_ix)$ is so called harmonic function which can be chosen as (Harrington, 2001)

$$f(k_ix)\sim\sin(k_ix),\cos(k_ix),\exp(jk_ix),\exp(-jk_ix). \tag{A3}$$

The parameters k_x, k_y, and k_z are wave numbers in x, y, and z directions. For the geometry shown in Fig. 8, to satisfy the boundary conditions at the conduction wall, we choose ψ in each region as

$$\begin{aligned}
\psi_1&=A_1\cos(k_{x0}x)\sin(\frac{n\pi y}{b})\sin(\frac{p\pi z}{c}),\\
\psi_2&=\{A_2\cos(k_{x1}x)+B_2\sin(k_{x1}x)\}\sin(\frac{n\pi y}{b})\sin(\frac{p\pi z}{c}),\\
\psi_3&=-A_1\cos[k_{x0}(x-a)]\sin(\frac{n\pi y}{b})\sin(\frac{p\pi z}{c}),
\end{aligned} \tag{A4}$$

where n and p are positive integers, A_1, A_2, and B_2 are coefficients. The parameters k_{x0} and k_{x1} in region 1, 3 and region 2 satisfy

$$\begin{aligned} k_{x0}^2 + (\frac{n\pi}{b})^2 + (\frac{p\pi}{c})^2 &= \omega^2\epsilon_0\mu_0, \\ k_{x1}^2 + (\frac{n\pi}{b})^2 + (\frac{p\pi}{c})^2 &= \omega^2\epsilon_1\mu_1, \end{aligned} \tag{A5}$$

where ϵ_0 and μ_0 are permittivity and permeability of air in region 1 and 3, while ϵ_1 and μ_1 are which of FR4 material in region 2. For TM to x modes, we choose the vector potential $\bar{A} = \hat{x}\psi$, then

$$\begin{aligned} \bar{E} &= \frac{\nabla\nabla\cdot\bar{A} + k^2\bar{A}}{j\omega\epsilon}, \\ \bar{H} &= \nabla\times\bar{A}, \end{aligned} \tag{A6}$$

which can be expanded in rectangular coordinates as

$$\begin{cases} E_x &= \frac{1}{j\omega\epsilon}\left(\frac{\partial^2}{\partial x^2} + k^2\right)\psi \\ E_y &= \frac{1}{j\omega\epsilon}\cdot\frac{\partial^2\psi}{\partial x\partial y} \\ E_z &= \frac{1}{j\omega\epsilon}\cdot\frac{\partial^2\psi}{\partial x\partial z} \end{cases}, \begin{cases} H_x &= 0 \\ H_y &= \frac{\partial\psi}{\partial z} \\ H_z &= -\frac{\partial\psi}{\partial y} \end{cases}. \tag{A7}$$

From equations (A4) and (A7), E_y in each region can be calculated as

$$\begin{aligned} E_{y1} &= -\frac{k_{x0}}{j\omega\epsilon_0}\frac{n\pi}{b}A_1\sin(k_{x0}x)\cos\left(\frac{n\pi y}{b}\right)\sin\left(\frac{p\pi z}{c}\right) \\ E_{y2} &= \frac{k_{x1}}{j\omega\epsilon_0}\frac{n\pi}{b}\{B_2\cos(k_{x1}x) - A_2\sin(k_{x1}x)\}\cos\left(\frac{n\pi y}{b}\right)\sin\left(\frac{p\pi z}{c}\right) \\ E_{y3} &= -\frac{k_{x0}}{j\omega\epsilon_0}\frac{n\pi}{b}A_1\sin[k_{x0}(a-x)]\cos\left(\frac{n\pi y}{b}\right)\sin\left(\frac{p\pi z}{c}\right). \end{aligned} \tag{A8}$$

Similarly, H_y in each region can be calculated as

$$\begin{aligned} H_{y1} &= \frac{p\pi}{c}A_1\cos(k_{x0}x)\sin\left(\frac{n\pi y}{b}\right)\sin\left(\frac{p\pi z}{c}\right) \\ H_{y2} &= \frac{p\pi}{c}\{A_2\cos(k_{x1}x) + B_2\sin(k_{x1}x)\}\sin\left(\frac{n\pi y}{b}\right)\sin\left(\frac{p\pi z}{c}\right) \\ H_{y3} &= -\frac{p\pi}{c}A_1\cos[k_{x0}(a-x)]\sin\left(\frac{n\pi y}{b}\right)\sin\left(\frac{p\pi z}{c}\right). \end{aligned} \tag{A9}$$

Continuity of E_y and H_y at $x = h_m$ requires $E_{y1}(h_m) = E_{y2}(h_m)$ and $H_{y1}(h_m) = H_{y2}(h_m)$. Hence,

$$\frac{-A_1k_{x0}}{\epsilon_0}\sin(k_{x0}h_m) = \frac{k_{x1}}{\epsilon_1}\{B_2\cos(k_{x1}h_m) - A_2\sin(k_{x1}h_m)\} \tag{A10}$$

$$A_1\cos(k_{x0}h_m) = A_2\cos(k_{x1}h_m) + B_2\sin(k_{x1}h_m). \tag{A11}$$

Also, the continuity of E_y and H_y at $x = h_m+d_m$ requires $E_{y3}(h_m+d_m) = E_{y2}(h_m+d_m)$ and $H_{y3}(h_m+d_m) = H_{y2}(h_m+d_m)$. Therefore,

$$\frac{-A_1k_{x0}}{\epsilon_0}\sin[k_{x0}(a-h_m-d_m)] = \frac{k_{x1}}{\epsilon_1}\{B_2\cos(k_{x1}h_m) - A_2\sin(k_{x1}h_m)\} \tag{A12}$$

$$-A_1\cos[k_{x0}(a-h_m-d_m)] = A_2\cos[k_{x1}(h_m+d_m)] + B_2\sin[k_{x1}(h_m+d_m)]. \tag{A13}$$

The summation of equation (A0) and (A12) provides

$$\begin{aligned} &\frac{-A_1k_{x0}}{\epsilon_0}\sin\left(k_{x0}\frac{a-d_m}{2}\right)\cos\left(k_{x0}\frac{a-2h_m-d_m}{2}\right) = \\ &\frac{k_{x1}}{\epsilon_1}\left[B_2\cos\left(k_{x1}\frac{2h_m+d_m}{2}\right) - A_2\sin\left(k_{x1}\frac{2h_m+d_m}{2}\right)\right]\cos\left(\frac{k_{x1}d_m}{2}\right). \end{aligned} \tag{A14}$$

The subtraction of equation (A11) from (A13) gives

$$A_1 \cos\left(k_{x0}\frac{a-d_m}{2}\right)\cos\left(k_{x0}\frac{a-2h_m-d_m}{2}\right) = \left[B_2\cos\left(k_{x1}\frac{2h_m+d_m}{2}\right) - A_2\sin\left(k_{x1}\frac{2h_m+d_m}{2}\right)\right]\sin\left(\frac{k_{x1}d_m}{2}\right). \tag{A15}$$

By dividing equation (A15) from (A14), the characteristic equation can be derived as

$$\frac{k_{x0}}{\epsilon_0}\tan\left(k_{x0}\frac{a-d_m}{2}\right) = \frac{k_{x1}}{\epsilon_1}\cot\left(\frac{k_{x1}d_m}{2}\right). \tag{A16}$$

By combining equations (A15) and (A16), we can derive a equation of k_{x0} as

$$\frac{k_{x0}}{\epsilon_0}\tan\left(k_{x0}\frac{a-d_m}{2}\right) = \frac{\sqrt{k_{x0}^2+C^2}}{\epsilon_1}\cot\left(\frac{d_m\sqrt{k_{x0}^2+C^2}}{2}\right), \tag{A17}$$

where $C^2 = \omega^2(\mu_1\epsilon_1 - \mu_0\epsilon_0)$. Also, from equation (A7), the E_x and E_y in region 3 are calculated as

$$\begin{aligned}(E_x)_{mnp} &= \frac{-(\omega^2\mu_0\epsilon_0 - (k_{x0})_m^2)A_1}{j\omega\epsilon_0}\cos[(k_{x0})_m(a-x)]\sin\left(\frac{n\pi y}{b}\right)\sin\left(\frac{p\pi z}{c}\right),\\ (E_y)_{mnp} &= \frac{-A_1(k_{x0})_m}{j\omega\epsilon_0}\frac{n\pi}{b}\sin[(k_{x0})_m(a-x)]\cos\left(\frac{n\pi y}{b}\right)\sin\left(\frac{p\pi z}{c}\right).\end{aligned} \tag{A18}$$

References

Afsharinejad, A., Davy, A., Jennings, B., & Brennan, C. (2015, April). An initial path-loss model within vegetation in the THz band. In *2015 9th european conference on antennas and propagation (eucap)* (p. 1-5).

Ai, Y., Cheffena, M., & Li, Q. (2015). Power delay profile analysis and modeling of industrial indoor channels. In *2015 9th european conference on antennas and propagation (eucap)* (p. 1-5).

Al-Hmood, H. (2017). A mixture gamma distribution based performance analysis of switch and stay combining scheme over shadowed fading channels. In *2017 annual conference on new trends in information communications technology applications (ntict)* (p. 292-297). doi: 10.1109/NTICT.2017.7976096

Brilliant.org. (n.d.). *Gaussian mixture model.* Retrieved from `https://brilliant.org/wiki/gaussian-mixture-model/`

Cheng, C., Kim, S., & Zajić, A. (2017, March). Comparison of path loss models for indoor 30 GHz, 140 GHz, and 300 GHz channels. In *2017 11th european conference on antennas and propagation (eucap)* (p. 716-720). doi: 10.23919/EuCAP.2017.7928124

Cheng, C., Kim, S., & Zajić, A. (2018, July). Study of diffraction at 30 GHz, 140 GHz, and 300 GHz. In *2018 ieee international symposium on antennas and propagation usnc/ursi national radio science meeting* (p. 1553-1554). doi: 10.1109/APUSNCURSINRSM.2018.8608803

Cheng, C., & Zajić, A. (2018, Sep.). Characterization of 300 GHz wireless channels for rack-to-rack communications in data centers. In *2018 ieee 29th annual international symposium on personal, indoor and mobile radio communications (pimrc)* (p. 194-198). doi: 10.1109/PIMRC.2018.8581042

Cheng, C.-L., Sangodoyin, S., & Zajić, A. (2020). Thz cluster-based modeling and propagation characterization in a data center environment. *IEEE Access*, *8*, 56544-56558. doi: 10.1109/ACCESS.2020.2981293

Communications, U. I. . (n.d.). *Phase locked dielectric resonator oscillator.* Retrieved from `https://www.ultra.group/media/2081/ultra-herley-series-pdro.pdf`

Electronics, D.-K. (n.d.-a). *Hex standoff threaded m5 nylon 0.787" (20.00mm).* Retrieved from https://www.digikey.com/en/products/detail/davies-molding-llc/SH1006-A/9990031

Electronics, D.-K. (n.d.-b). *Hex standoff threaded m5 nylon 1.969" (50.00mm).* Retrieved from https://www.digikey.com/en/products/detail/davies-molding-llc/SH1006-G/9990037

Fricke, A., Achir, M., Le Bars, P., & Kürner, T. (2015, Sep.). Characterization of transmission scenarios for terahertz intra-device communications. In *2015 ieee-aps topical conference on antennas and propagation in wireless communications (apwc)* (p. 1137-1140). doi: 10.1109/APWC.2015.7300195

Fricke, A., Kürner, T., Achir, M., & Bars, P. L. (2017, March). A model for the reflection of terahertz signals from printed circuit board surfaces. In *2017 11th european conference on antennas and propagation (eucap)* (p. 711-715). doi: 10.23919/EuCAP.2017.7928148

Fricke, A., Rey, S., Achir, M., Le Bars, P., Kleine-Ostmann, T., & Kürner, T. (2013, Sep.). Reflection and transmission properties of plastic materials at THz frequencies. In *2013 38th international conference on infrared, millimeter, and terahertz waves (irmmw-thz)* (p. 1-2). doi: 10.1109/IRMMW-THz.2013.6665413

Fu, J., Juyal, P., & Zajić, A. (2019a, March). 300 GHz channel characterization of chip-to-chip communication in metal enclosure. In *2019 13th european conference on antennas and propagation (eucap)* (p. 1-5).

Fu, J., Juyal, P., & Zajić, A. (2019b). THz channel characterization of chip-to-chip communication in desktop size metal enclosure. *IEEE Transactions on Antennas and Propagation*, 1-1. doi: 10.1109/TAP.2019.2934908

Fu, J., Juyal, P., & Zajić, A. (2020). Modeling of 300 ghz chip-to-chip wireless channels in metal enclosures. *IEEE Transactions on Wireless Communications*, *19*(5), 3214-3227. doi: 10.1109/TWC.2020.2971206

Fu, J., Juyal, P., & Zajić, A. (2021). Near field modeling for thz wireless channel in nettop size metal enclosures. In *2021 15th european conference on antennas and propagation (eucap)* (p. 1-5). doi: 10.23919/EuCAP51087.2021.9411127

Harrington, R. F. (2001). Plane wave functions. In *Time-harmonic electromagnetic fields* (p. 143-197). doi: 10.1109/9780470546710.ch4

He, D., Guan, K., Fricke, A., Ai, B., He, R., Zhong, Z., ... Kürner, T. (2017, Sep.). Stochastic channel modeling for kiosk applications in the terahertz band. *IEEE Transactions on Terahertz Science and Technology*, *7*(5), 502-513. doi: 10.1109/TTHZ.2017.2720962

Inc., W. (n.d.). *Uxcell brass m2.5 14mm+6mm male-female hex standoff.* Retrieved from https://www.walmart.com/ip/Uxcell-Brass-M2-5-14mm-6mm-Male-Female-Hex-Standoff-50-Pack/724184483

Jacob, M., Priebe, S., Dickhoff, R., Kleine-Ostmann, T., Schrader, T., & Kürner, T. (2012, March). Diffraction in mm and sub-mm wave indoor propagation channels. *IEEE Transactions on Microwave Theory and Techniques*, *60*(3), 833-844. doi: 10.1109/TMTT.2011.2178859

Jornet, J. M., & Akyildiz, I. F. (2011, October). Channel modeling and capacity analysis for electromagnetic wireless nanonetworks in the terahertz band. *IEEE Transactions on Wireless Communications*, *10*(10), 3211-3221. doi: 10.1109/TWC.2011.081011.100545

Khalid, N., & Akan, O. B. (2016). Wideband THz communication channel measurements for 5G indoor wireless networks. In *Communications (icc), 2016 ieee international conference on* (pp. 1–6).

Kim, S., & Zajić, A. (2015, April). Statistical modeling of THz scatter channels. In *2015 9th european conference on antennas and propagation (eucap)* (p. 1-5).

Kim, S., & Zajić, A. (2016). Characterization of 300-GHz wireless channel on a computer motherboard. *IEEE Transactions on Antennas and Propagation*, *64*(12),

5411–5423.

Kim, S., & Zajić, A. (2016, Sep.). Statistical modeling and simulation of short-range device-to-device communication channels at sub-THz frequencies. *IEEE Transactions on Wireless Communications*, *15*(9), 6423-6433. doi: 10.1109/TWC.2016.2585103

Kim, S., & Zajić, A. G. (2015). Statistical characterization of 300-GHz propagation on a desktop. *IEEE Transactions on Vehicular Technology*, *64*(8), 3330–3338.

Kleine-Ostmann, T., Jastrow, C., Priebe, S., Jacob, M., Kürner, T., & Schrader, T. (2012, July). Measurement of channel and propagation properties at 300 GHz. In *2012 conference on precision electromagnetic measurements* (p. 258-259). doi: 10.1109/CPEM.2012.6250900

Kürner, T. (2018, Oct). THz communications: Challenges and applications beyond 100 Gbit/s. In *2018 international topical meeting on microwave photonics (mwp)* (p. 1-4). doi: 10.1109/MWP.2018.8552889

Kürner, T., Fricke, A., Rey, S., Le Bars, P., Mounir, A., & Kleine-Ostmann, T. (2015). Measurements and modeling of basic propagation characteristics for intra-device communications at 60 ghz and 300 GHz. *Journal of Infrared, Millimeter, and Terahertz Waves*, *36*(2), 144–158.

Meijerink, A., & Molisch, A. F. (2014). On the physical interpretation of the salehvalenzuela model and the definition of its power delay profiles. *IEEE Transactions on Antennas and Propagation*, *62*(9), 4780-4793. doi: 10.1109/TAP.2014.2335812

Millimeter, N. (n.d.). *Frequency multiplier - 33 to 50 gh.* Retrieved from `https://nordengroup.com/product-group/frequency-multiplier-33-to-50-ghz/`

Piesiewicz, R., Jansen, C., Mittleman, D., Kleine-Ostmann, T., Koch, M., & Kürner, T. (2007, Nov). Scattering analysis for the modeling of THz communication systems. *IEEE Transactions on Antennas and Propagation*, *55*(11), 3002-3009. doi: 10.1109/TAP.2007.908559

Priebe, S., Jacob, M., Jansen, C., & Kürner, T. (2011, April). Non-specular scattering modeling for THz propagation simulations. In *Proceedings of the 5th european conference on antennas and propagation (eucap)* (p. 1-5).

Priebe, S., Jacob, M., Jastrow, C., Kleine-Ostmann, T., Schrader, T., & Kürner, T. (2010, Sept). A comparison of indoor channel measurements and ray tracing simulations at 300 GHz. In *35th international conference on infrared, millimeter, and terahertz waves* (p. 1-2). doi: 10.1109/ICIMW.2010.5612330

Priebe, S., Jacob, M., & Kürner, T. (2014, March). Angular and rms delay spread modeling in view of THz indoor communication systems. *Radio Science*, *49*(3), 242-251. doi: 10.1002/2013RS005292

Priebe, S., Jastrow, C., Jacob, M., Kleine-Ostmann, T., Schrader, T., & Kürner, T. (2011). Channel and propagation measurements at 300 GHz. *IEEE Transactions on Antennas and Propagation*, *59*(5), 1688–1698.

Priebe, S., & Kürner, T. (2013, Sep.). Stochastic modeling of THz indoor radio channels. *IEEE Transactions on Wireless Communications*, *12*(9), 4445-4455. doi: 10.1109/TWC.2013.072313.121581

Schneider, T., Wiatrek, A., Preussler, S., Grigat, M., & Braun, R. (2012, March). Link budget analysis for terahertz fixed wireless links. *IEEE Transactions on Terahertz Science and Technology*, *2*(2), 250-256. doi: 10.1109/T{THz}.2011.2182118

Statista. (2019). *Data volume of internet of things (iot) connections worldwide in 2019 and 2025.* Retrieved from `https://www.statista.com/statistics/1017863/worldwide-iot-connected-devices-data-size/`

Statista. (2021). *Number of internet of things (iot) connected devices worldwide from 2019 to 2030.* Retrieved from `https://www.statista.com/statistics/1194682/iot-connected-devices-vertically/`

Stüber, G. L., & Steuber, G. L. (1996). *Principles of mobile communication* (Vol. 2).

Springer.

Tekbıyık, K., Ekti, A. R., Kurt, G. K., & Görçin, A. (2019). Terahertz band communication systems: Challenges, novelties and standardization efforts. *Physical Communication*, *35*, 100700.

Tekbıyık, K., Ekti, A. R., Kurt, G. K., Grin, A., & Yarkan, S. (2021). Modeling and analysis of short distance sub-terahertz communication channel via mixture of gamma distribution. *IEEE Transactions on Vehicular Technology*, *70*(4), 2945-2954. doi: 10.1109/TVT.2021.3063209

Virginia Diodes, I. (n.d.-a). *Custom transmitters.* Retrieved from `https://vadiodes.com/en/products/custom-transmitters`

Virginia Diodes, I. (n.d.-b). *Mixers - vdi model: Wr2.8shm.* Retrieved from `https://www.vadiodes.com/en/wr2-8shm`

Virginia Diodes, I. (n.d.-c). *Multipliers - vdi model: Wr6.5x3.* Retrieved from `https://www.vadiodes.com/en/wr6-5x3`